Monthly Notices of the ROYAL ASTRONOMICAL SOCIETY

MNRAS **544,** 4702–4721 (2025) https://doi.org/10.1093/mnras/staf1790
Advance Access publication 2025 October 21

A multiwavelength view of the outflowing short-period X-ray binary UW CrB

S. Fijma [1]★ N. Degenaar [1] N. Castro Segura [2,3] T. J. Maccarone,[4] C. Knigge [3] M. Armas Padilla [5,6] D. Mata Sánchez [5,6] T. Muñoz-Darias [5,6] J. V. Hernández Santisteban [7] L. Rhodes [8,9,10] J. Bright [8,11] J. van den Eijnden [1] and D. A. Green [12]

[1]*Anton Pannekoek Institute for Astronomy, University of Amsterdam, Science Park 904, NL-1098 XH, Amsterdam, the Netherlands*
[2]*Department of Physics, University of Warwick, Coventry CV4 7AL, UK*
[3]*Department of Physics & Astronomy, University of Southampton, Southampton SO17 1BJ, UK*
[4]*Department of Physics & Astronomy, Texas Tech University, Box 41051, Lubbock, TX 79409-1051, USA*
[5]*Instituto de Astrofísica de Canarias, E-38205 La Laguna, Tenerife, Spain*
[6]*Departamento de Astrofísica, Univ. de La Laguna, E-38206 La Laguna, Tenerife, Spain*
[7]*SUPA School of Physics & Astronomy, University of St Andrews, North Haugh, St Andrews KY16 9NS, Scotland, UK*
[8]*Department of Physics, Astrophysics, University of Oxford, Denys Wilkinson Building, Keble Road, Oxford OX1 3RH, UK*
[9]*Department of Physics, McGill University, 3600 University Street, Montreal, QC H3A 2A7, Canada*
[10]*Trottier Space Institute at McGill, 3550 University Street, Montreal, QC H3A 2T8, Canada*
[11]*Breakthrough Listen, Astrophysics, Department of Physics, The University of Oxford, Keble Road, Oxford OX1 3RH, UK*
[12]*Astrophysics Group, Cavendish Laboratory, 19 J. J. Thomson Avenue, Cambridge CB3 0HE, UK*

Accepted 2025 September 8. Received 2025 August 18; in original form 2025 June 4

ABSTRACT

Previous work detected transient ultraviolet outflow features for the short-period ($P_{orb}\approx111$ min), low-mass X-ray binary (LMXB) UW CrB, suggesting the presence of a disc wind in the system. However, because of the transient nature of the outflow features, and the limited amount of data available, the features were challenging to interpret. To follow up on this work, we present a comprehensive multiwavelength campaign on UW CrB. We observe complex phenomenology and find several features that could be naturally interpreted as being associated with a persistent disc wind. Moreover, we identify a blue-shifted absorption in the H β line during one of the epochs, which might be the signature of such an outflow. We present an X-ray to radio campaign of the source, discuss our results in the context of accretion disc wind outflows, present a 'toy model' interpretation of the outflow scattering the X-ray emission into our line of sight, and explore the implications for binary evolution models. If correct, our preferred scenario of a persistent disc wind suggests that mass transfer for LMXBs can be non-conservative down to short orbital periods, and thereby opens an important parameter space for angular momentum loss in compact binaries.

Key words: accretion, accretion discs – binaries: eclipsing – stars: neutron – stars: winds, outflows – X-rays: binaries.

1 INTRODUCTION

1.1 X-ray binaries and their outflows

Multiwavelength observing campaigns are instrumental in improving our understanding of the outflows and the evolution of binaries containing a compact object. X-ray binaries in particular consist of a compact object, either a neutron star (NS) or a black hole (BH), and a companion star. For low-mass X-ray binaries (LMXBs), the companion star is less massive than the compact object, i.e. around $\lesssim1M_{\odot}$ for an NS-LMXB. The compact object accretes material from this companion star through Roche lobe overflow, forming an accretion disc (see e.g. C. Done, M. Gierliński & A. Kubota 2007, for a review). The emission from the accretion flow can be detected in the near-infrared (NIR), optical, ultraviolet (UV), and X-ray bands. LMXBs can also launch powerful outflows. These systems exhibit collimated jets, whose emission can dominate in the radio, millimeter and potentially the infrared band. Moreover, vast amounts of material can be lost from the disc in the form of accretion disc winds (some predictions range from $2-15\times\dot{M}_{\rm acc}$; e.g. J. Neilsen & J. C. Lee 2009; G. Ponti et al. 2012; N. Higginbottom et al. 2017), which can be detected from NIR to X-ray wavelengths.

Disc wind outflows are proposed to carry away a lot of mass and angular momentum (e.g. J. Neilsen 2013; J. M. Miller et al. 2015; J. V. Hernández Santisteban et al. 2019). This may affect the accretion process (e.g. M. C. Begelman & C. F. McKee 1983; T. Muñoz-Darias et al. 2016; B. E. Tetarenko et al. 2018), and potentially even regulate changes in the spectral states of LMXBs (e.g. G. A. Shields et al. 1986; N. Higginbottom et al. 2019). Moreover, with angular momentum loss, the long-term orbital evolution of the binary can be altered (e.g. N. Degenaar et al. 2014; A. Marino et al. 2019).

★ E-mail: s.c.fijma@uva.nl

Recent studies have shown that disc winds in binary systems are also highly impactful for population studies and predicting orbital separations, which in turn, impacts the rates and merger time of compact object binaries (M. Gallegos-Garcia, J. Jacquemin-Ide & V. Kalogera 2024).

Furthermore, predictions show that typical LMXBs should produce relatively massive neutron stars through conservative mass transfer, and potentially cause neutron stars to collapse into black holes (e.g. J. C. Siegel et al. 2023), but we observe neutron stars with masses above 1.4 $M_{\odot}$ relatively infrequently (e.g. F. Özel & P. Freire 2016). This suggests that accretion disc winds may severely limit the mass gain of compact objects in LMXBs. Finally, outflows from LMXBs are proposed to heat and stir up the surrounding interstellar medium, possibly affecting star formation (e.g. R. P. Fender, T. J. Maccarone & Z. van Kesteren 2005; S. Justham & K. Schawinski 2012). Studying LMXB outflows is thus vital for gaining a deeper understanding of compact object binaries and how they evolve, as well as accretion physics and LMXB feedback.

Three basic mechanisms have been proposed to launch disc winds. First, thermal driving likely contributes to launching winds in most LMXBs (e.g. M. C. Begelman & C. F. McKee 1983; D. T. Woods et al. 1996; D. Proga & T. R. Kallman 2002). Here, the upper layers of the accretion disc are heated by X-ray emission from the inner disc and hot inner flow (i.e. the corona), causing them to puff up. Beyond a critical radius (at around 10 per cent of the Compton radius R_{IC}; e.g. M. C. Begelman & C. F. McKee 1983), the gas can be heated sufficiently to unbound when the thermal velocity exceeds the local escape velocity (e.g. M. Díaz Trigo & L. Boirin 2016; N. Higginbottom et al. 2017). Secondly, radiative driving may be important in some LMXBs. For LMXBs with an accretion rate near the Eddington luminosity (L_{EDD}), radiation pressure of electron scattering can contribute to thermal driving in launching disc winds (e.g. V. Icke 1980; I. Shlosman, P. A. Vitello & G. Shaviv 1985; D. Proga & T. R. Kallman 2002). Finally, magnetic driving can also launch outflows, as magnetic field lines thread the accretion disc and are expected to accelerate gas via magnetocentrifugal forces (e.g. R. D. Blandford & D. G. Payne 1982; R. T. Emmering, R. D. Blandford & I. Shlosman 1992; J. Ferreira 1997; J. M. Miller et al. 2006; S. Chakravorty et al. 2016; K. Fukumura et al. 2017)

Smoking-gun evidence for disc winds in LMXBs was initially discovered via blue-shifted X-ray absorption lines, probing hot ionized gas outflows originating from the disc (e.g. Y. Ueda et al. 1998, 2004; J. M. Miller et al. 2006), following indirect evidence in earlier works (e.g. M. C. Begelman & C. F. McKee 1983; T. Oosterbroek et al. 1997). Recent discoveries of optical, UV, and even NIR winds (e.g. R. M. Bandyopadhyay et al. 1999; N. Castro Segura et al. 2022; V. A. Cúneo et al. 2020; J. Sánchez-Sierras & T. Muñoz-Darias 2020; D. Mata Sánchez et al. 2022; T. Muñoz-Darias et al. 2016; F. Rahoui, M. Coriat & J. C. Lee 2014) have shown that X-ray binaries can harbour lower-ionization outflowing material as well. Wind signatures seen at these lower energies include blue-shifted absorption lines and P-Cygni profiles, extended emission wings, as well as broadened, flat-topped and/or asymmetric red-skewed line profiles.

As for their properties, velocities of disc winds range from a few hundred to a few thousand km s^{-1}(e.g. J. Neilsen & N. Degenaar 2023). Most disc winds have been detected in intermediate to high inclination systems (e.g. G. Ponti et al. 2012). This is proposed to be due to the highest densities of the outflow being near the disc plane (i.e. equatorial), causing observable absorption features being preferentially observed at higher inclinations, although the outflow itself is proposed to be quasi-spherical (e.g. N. Higginbottom et al. 2019). Furthermore, disc winds have been identified in LMXBs with wide orbital periods (often exceeding $P_{orb} \gtrsim 20$ h; e.g. M. Díaz Trigo & L. Boirin 2016; G. Panizo-Espinar et al. 2022; J. Neilsen & N. Degenaar 2023). As the orbital period (as well as the mass ratio) dictates the size of the accretion disc, most observational evidence points to thermal driving being the main contributing mechanism in launching winds. Therefore, the discovery of an UV outflow in a short period X-ray binary with a relatively small accretion disc, UW CrB (UW Coronae Borealis), came as a surprise (S. Fijma et al. 2023).

1.2 The short-period X-ray binary UW CrB

UW CrB or MS 1603.6+2600, is an LMXB that was discovered by S. L. Morris et al. (1990) with the *Einstein Observatory* X-ray telescope at a flux level of $f_X \approx 1 \times 10^{-12}$ erg s^{-1} cm^{-2} (0.3–3.5 keV; I. M. Gioia et al. 1990, without correction for absorption). The compact object was confirmed to be a neutron star via the discovery of type-I bursts (i.e. Type-I X-ray bursts; see review in e.g. D. K. Galloway & L. Keek 2021), which have been detected in X-ray (e.g. K. Mukai et al. 2001; P. Hakala et al. 2005), optical (e.g. R. I. Hynes, E. L. Robinson & E. Jeffery 2004; P. Muhli et al. 2004; P. Hakala et al. 2009; M. R. Kennedy et al. 2024) and UV observations (S. Fijma et al. 2023). Based on the eclipses seen in optical and X-ray light curves, the inclination is estimated to be $77^{\circ} \leq i \leq 88^{\circ}$ (e.g. P. Hakala et al. 2005; P. A. Mason et al. 2008). The source is a persistently accreting LMXB, and based on its orbital period and measured optical brightness, it is proposed to accrete at around 1−10 per cent L_{EDD} (e.g. S. Fijma et al. 2023), which is consistent with the amplitude, recurrence rate and duration of the detected type-I bursts. The source has an orbital period of $P_{orb} = 110.98$ min, as well as a non-eclipse modulation period of P = 112.6 min (P. A. Mason et al. 2008). The latter period is probably associated with 'superhump-like' variations, i.e. it is the beat-period between the orbit and a super-orbital period of 5.5 d. This superorbital period is thought to be associated with the (prograde) precessing period of UW CrB's non-axisymmetric elliptical disc (e.g. P. A. Mason et al. 2008; P. Hakala et al. 2009).

The source is located out of the Galactic plane (b=+46.8°), and the interstellar extinction towards it is relatively low based on a H I survey ($N_H = 4 \times 10^{20}$ cm^{-2}; HI4PI Collaboration 2016) and X-ray spectral modelling ($N_H \approx 1 \times 10^{21}$ cm^{-2}; K. Mukai et al. 2001; P. G. Jonker et al. 2003; P. Hakala et al. 2005). Based on the observed optical properties and the brightness of the type-I bursts, P. G. Jonker et al. (2003) propose that UW CrB is an accretion disc corona source (ADC), where we are viewing the LMXB nearly edge-on. This means that the inner region and compact object are obscured, and subsequently all the X-ray emission is scattered into our line of sight by a scattering medium, reducing the observed X-ray flux. This scenario is further supported by P. Hakala et al. (2005), who estimate a minimum distance of ≈6 kpc, based on the peak brightness of the type-I bursts.

S. Fijma et al. (2023) detected an outflow in archival far-UV (FUV) spectra of UW CrB. The 'smoking gun' outflow signatures were P-Cygni profiles in the Si IV and N V spectral lines. The terminal velocity of the outflow, suggested by the P-Cygni profiles, is around ≈1500 km s^{-1}, consistent with the typical detected speed of disc winds (e.g. J. Neilsen & N. Degenaar 2023). S. L. Morris et al. (1990) briefly mention blue-shifted He I lines in optical spectra of UW CrB as well, suggesting an optical outflow, but the authors did not discuss this further. The reason why the detection of the outflow was surprising, is because the accretion disc was initially considered

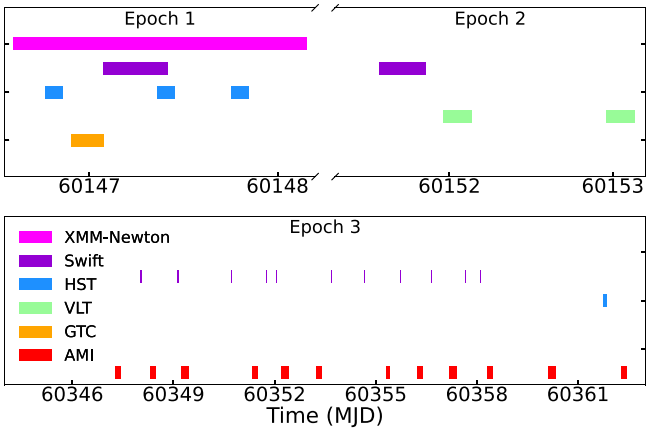

Figure 1. A schematic diagram showing the scheduling of the multi-wavelength observing campaign for UW CrB. The *Swift* observing windows in Epoch 1 and 2 consist of 4 snapshots each, but are depicted as continuous blocks for clarity.

to be too small to be able to launch a wind via thermal driving, and radiation pressure due to electron scattering was also not expected to be sufficiently strong in this system. However, by modelling the thermal stability curves of the disc atmosphere, S. Fijma et al. (2023) show that a thermal wind *can* be launched in this system, due to the heating of the upper disc layers by the neutron star's black body radiation.

The detected P-Cygni profiles also appear to be transient on ≈15 min time-scales, as they were only detected in one 15 min sub-exposure, and not in the exposure directly preceding it. It is unclear if this transient nature is intrinsic to the outflow, or if it could be a line-of-sight (i.e. visibility) effect. Based on the transient nature of the signatures, as well as the orbital phase where the outflow was detected ($\phi \approx 0.7-0.8$), other scenarios were considered as well, such as ablation of the companion star (e.g. E. M. Ratti et al. 2012; A. H. Knight et al. 2022), or an outflow launched from the point where the accretion stream impacts the disc (the impact point or hot spot; e.g. I. Psaradaki et al. 2018).

In order to confirm the origin of the outflow and characterize its properties, we performed a follow up multiwavelength observing campaign. We describe our observations in Section 2, present our results in Sections 3 and 4, and discuss the nature of the outflow in Section 5.

2 OBSERVATIONS

For our observing campaign, we had three observing windows, namely July 21–22, 2023 (Epoch 1), July 26–28, 2023 (Epoch 2), and February 7–22, 2024 (Epoch 3). In Fig. 1 and Table 1, we show an overview of the observing details. Below, we describe the observations for each facility.

2.1 *XMM–Newton*

XMM–Newton (*X-ray Multi-Mirror Mission Newton*) observed UW CrB from July 21 to 23, 2023, resulting in 121 ks of total exposure time. We reduced the data using the Science Analysis Software (SAS) v20. We extract spectra and light curves using the standard analysis threads[1]. We used an extraction region for the source at the right ascension (RA) and declination (Dec.) of RA = $16^h05^m45^s.80$ and Dec.=$+25^\circ51'43''.98$, and for the background region at RA = $16^h05^m35^s.92$ and Dec. = $+25^\circ51'43''.95$, both with a radius of 30 arcsec. In order to create time-resolved spectra, we extract data from the desired time-intervals using TABGTIGEN.

The EPIC-pn (European Photon Imaging Camera) data were recorded using Large window mode. We evaluate the background flaring during the observation, and exclude flaring above RATE ≥ 0.4. We analyse the spectra from 0.2 to 10 keV. For the RGS (Reflection Grating Spectrometer) instrument, after visually inspecting that the two detectors RGS 1 and 2 are consistent, we combine the spectra of both detectors per order. Furthermore, we inspect where the background and target spectra overlap, and remove these sections in the analysis. For the spectra using all the data, we analyse the data between 6.4–27 Å (0.5–1.9 keV) for the first order, and 7–16 Å (0.8–1.8 keV) for the second order. For the time-resolved spectra, we analyse the data between 6.4–17 Å (0.7–1.9 keV) for the first order spectra.

To analyse the X-ray spectra, we use XSPEC (v12.11.0; K. A. Arnaud 1996). We set the abundances based on J. Wilms, A. Allen & R. McCray (2000) and the cross-sections based on D. A. Verner et al. (1996). To determine the goodness-of-fit and the best-fitting spectral parameters, we use the χ^2-statistic for the EPIC-pn spectra, and the C-statistic for the RGS spectra. We determine the significance of lines in the continuum model using the normalization divided by the 1σ uncertainty on the normalization (N/σ_N), in both the RGS and EPIC-pn spectra.

2.2 *HST*

The *Hubble Space Telescope* (*HST*) observed UW CrB in four visits of two orbits each. The first three visits were carried out simultaneously with the *XMM–Newton* observation, between July 21 to 22, 2023. The fourth visit was scheduled at a later date, on February 21, 2024. The total exposure time with *HST* was 17 ks. The data were obtained using the Cosmic Origins Spectrograph (COS; J. C. Green et al. 2012) in TIME-TAG mode using the primary science aperture. The spectral data were recorded with the G140L grating (covering around 1100 to 2300 Å; R≈2000) with a central wavelength of 1105 Å.

During Visit 2, the Fine Guidance Sensors on *HST* could not acquire the guide stars, meaning that the data obtained were taken under gyro pointing control. The exposures recorded during the first orbit were significantly affected, since the COS processed data files did not contain data of our target. The exposures recorded during the second orbit did contain data of the target, but it is not guaranteed that the timing or flux properties are reliable. In order to investigate if the data taken during this orbit are consistent with the previous and following orbits, we inspected the Corrected Events Lists (CORRTAG) data. From the CORRTAG files, we compared the trace from visit 2 with the other visits in the 2D-images. Moreover, we created and compared histograms of each recorded trace. We found that the quality of the exposures in visit 2 appears consistent with the exposures from visits 1 and 3. The spectra obtained in visit 2 are also consistent with those obtained in the other visits, in terms of the broad-band flux and detected emission lines. Therefore, we decide to include the spectra from visit 2 in our analysis, and approach interpretation of this data set with caution. Because of the guide star acquisition failure affecting visit 2, we were awarded an additional fourth visit with *HST*, which was carried out in February 21, 2024.

[1] https://www.cosmos.esa.int/web/xmm-newton/sas-threads

Table 1. Observation summary.

Telescope	Instrument(s)	Obs/run ID(s)	Start time (UT)	End time (UT)	Wavelength range	Total exposure time (ks)
			Epoch 1			
XMM-Newton	EPIC-pn, RGS	0 924 010 101	2023-07-21 14:11:34	2023-07-23 03:41:34	0.2–12 keV	121 ks
Swift	XRT, UVOT	00 035 060 015	2023-07-22 01:42:56	2023-07-22 09:58:33	0.3–10 keV	2.6 ks
HST visit 1	COS	LF3G01010	2023-07-21 18:20:01	2023-07-21 20:34:39	1160–2235 Å	4.9 ks
HST visit 2	COS	LF3G02010	2023-07-22 08:35:32	2023-07-22 10:50:10	1161–2235 Å	2.6 ks
HST visit 3	COS	LF3G03010	2023-07-22 18:05:52	2023-07-22 20:20:30	1162–2235 Å	4.9 ks
GTC	OSIRIS	-	2023-07-22 21:39:15	2023-07-23 02:04:40	3630–7000 Å	15 ks
			Epoch 2			
Swift	XRT, UVOT	00 035 060 016	2023-07-26 13:39:56	2023-07-26 20:31:40	0.3–10 keV	2.8 ks
VLT obs 1	XShooter	0111.D-2426(A)	2023-07-26 23:02:16	2023-07-27 03:13:31	3000–25000 Å	14 ks
VLT obs 2	XShooter	0111.D-2426(A)	2023-07-28 23:02:21	2023-07-27 03:09:36	3000–25000 Å	14 ks
			Epoch 3			
AMI obs 1–12		-	2024-02-07 06:30	2024-02-22 11:32	15.5 GHz	196 ks
Swift obs 1–12	XRT, UVOT	00035060017-00 035 060 028	2024-02-08 00:13:00	2024-02-19 00:38:20	0.3–10 keV	11 ks
HST visit 4	COS	LF3G04010	2024-02-21 18:04:06	2024-02-21 20:18:14	1160–2235 Å	4.8 ks

We use the *HST* CalCOS pipeline[2] to reduce the data. As the spectra contain airglow lines, we mask the strongest lines, i.e. the geocoronal Lyman α (1208−1225 Å) and O I (1298−1312 Å) lines, in our analysis. We use standard pipeline data products to obtain one-dimensional spectra per exposure. As described in S. Fijma et al. (2023); we resample the one-dimensional spectra on to a common wavelength grid using adapted code from the SPECTRES package (A. C. Carnall 2017). We extract light curves from the TIME-TAG events lists following the procedure described in N. Castro Segura et al. (2022), using a modified version of the LIGHTCURVE[3] package. Finally, we use the COSTOOLS SPLITTAG package to split the TIME-TAG data into time-resolved spectra for the desired time intervals.

2.3 GTC

The Gran Telescopio Canarias (GTC) observed UW CrB simultaneously with *XMM–Newton* from July 22 to 23, 2023, resulting in a continuous spectroscopic dataset of 4.2 h (or ≈15 ks) of total exposure time. The data were recorded using the OSIRIS (Optical System for Imaging and low Resolution Integrated Spectroscopy) instrument for long slit spectroscopy, with a slit width of 1″, 2×2 binning, using the fast readout mode.

The target was first observed for 12 exposures of 1182s each with the R2500R grism (R≈2475; 5575−7685 Å), in order to obtain detailed exposures of the Hα and He I 5876 Å lines, which are sensitive to outflows (e.g. T. Muñoz-Darias et al. 2016). One more exposure was recorded with the R1000B grism (R≈1018; 3630−7000 Å), in order to cover a larger wavelength range. The latter allows us to measure the He II 4686 Å line, which allows us to study the intrinsic EUV flux. We reduced the data using Gemini IRAF v1.15, and apply the barycentric correction to all analysed spectra.

2.4 VLT

The Very Large Telescope (VLT) observed UW CrB in Epoch 2, as it could not observe simultaneously with the other telescopes due to technical constraints. The data was recorded on two consecutive nights, on July 26 and 27, 2023. The target was observed using the XShooter instrument, where the UVB (3000–5600 Å), VIS (5500–10 000 Å), and NIR (10 000–25 000 Å) arms are recorded simultaneously. A binning of 1×2 and the 1pt/400k/lg readout mode were used, with slit widths of 1, 0.9, and 0.9 arcsec for the UVB, VIS, and NIR arms, respectively. The individual exposure times are 260, 238, and 250 s, for the UVB, VIS, and NIR arms, respectively. The exposures were arranged in AB pairs alternating between source and sky positions. We used a nod throw length of 5 arcsec to nod on the slit. The total exposure times are between 7.3 h (≈26 ks) and 7.7 h (≈28 ks) per arm.

We reduced the data using the ESO Reflex pipeline v2.11.5. We follow the standard procedure for NODDING mode data in order to obtain the flux-calibrated combined UVB, VIS, and NIR spectra for each night. In order to reduce the spectra from the individual exposures, we reduce the data using the STARE mode procedure, as recommended by the XShooter manual. As this will not correct for the nodding on the slit, we identify the location of the trace during the data reduction, and change the LOCALIZE-SLIT-POSITION parameter to the position of the target on the slit accordingly. We apply the barycentric correction to all analysed spectra. Finally, we resample the one-dimensional spectra onto a common wavelength grid where needed to increase the signal-to-noise ratio (SNR), using the same code as described in Section 2.2.

2.5 AMI-LA

The Arcminute Microkelvin Imager Large Array (AMI-LA; J. T. L. Zwart et al. 2008; J. Hickish et al. 2018) radio telescope observed UW CrB during Epoch 3. The source was observed every day for around 4–5 h from February 7 to 22, 2024, resulting in a total exposure time of around 55 h. The data were recorded at a central frequency of 15.5 GHz with a bandwidth of 5 GHz. The data was reduced using a custom pipeline (REDUCE_DC; Y. C. Perrott et al. 2013), using 3C286 and J1602+3326 as the bandpass and phase calibrators, respectively. Finally, the data were cleaned and imaged in CASA (Version 4.7.0; J. P. McMullin et al. 2007).

2.6 *Swift XRT* and *UVOT*

For Epoch 1, 2, and 3, *Swift* monitored UW CrB in order to compare the X-ray and UV flux level of the source between

[2]https://github.com/spacetelescope/calcos
[3]https://github.com/justincely/lightcurve

observing windows. As there is a 7.3 ks *Swift* archival observation available that was recorded simultaneously with the *HST* data from 2012 described in the discovery of the UV outflow (S. Fijma et al. 2023), this allows us to compare our observing campaign to the 2012 observing campaign. Moreover, *Swift* recorded quasi-simultaneous exposures with AMI, so we can compare the X-ray/radio behaviour in time. In total, *Swift* recorded 14 exposures of UW CrB. All the exposures with the *X-Ray Telescope* (*XRT*; D. N. Burrows et al. 2005) were taken in photon counting (PC) mode.

The two exposures taken in Epoch 1 and 2 were around 3 ks each. The mode of the Ultraviolet and Optical Telescope (UVOT; P. W. A. Roming et al. 2005) for these exposures allowed us to measure the brightness in all UVOT bands (u, b, v, $uvw1$, $uvw2$, and $uvm2$) For Epoch 3, 12 exposures of 1 ks each were recorded. The UVOT mode for these exposures only included u and $uvw2$, due to the shorter observing time, so we only have information about the UV brightness.

The *Swift/XRT* spectra were reduced using The *Swift-XRT* data products generator[4] (P. A. Evans et al. 2007). We analyse the spectra between 0.3–10 keV using XSPEC, as described for *XMM-Newton*. The *Swift*/*UVOT* data are reduced using the *Swift* UVOT software as part of the HEASOFT software package v6.34, using standard data analysis prescriptions[5]. We first sum all the extensions using UVOTIMSUM and extract the source data using UVOTSOURCE, using a source region of 8″ at R.A.=$16^{h}05^{m}45\overset{s}{.}87s$ and DEC=+25°51′45″.25, and a background region of 15″ at RA = $16h05m51.39s$ and Dec.=+25d51′08″.78.

3 MULTIBAND SPECTRA

3.1 The X-ray spectra

3.1.1 EPIC-pn

In order to model the full 0.2–10 keV EPIC-pn spectrum, we initially attempt a simple absorbed black body + power-law model as used in P. J. Hakala et al. (1998) and P. G. Jonker et al. (2003) for *ROSAT* (Röntgensatellit) and *Chandra* spectra, respectively. However, we find that this does not fit the data well, with a corresponding χ^2 value of 2561 and 1956 degrees-of-freedom (dofs). While adding a broad Gaussian in the Fe–K region improves the fit, i.e. at 6.76 keV, significant residuals are still present, most prominently near 0.5 and 1 keV. This would be around the wavelength ranges of prominent emission lines such as N VII at 0.5 keV (or 25 Å), O VIII at 0.8 keV (or 14.7 Å), and Ne X at 1 keV (or 12.1 Å). Like P. Hakala et al. (2005), we find that we need to include the MEKAL model component in our continuum model. Using FTEST to test the F-statistic and its probability, we obtain a significantly improved model when adding the MEKAL model component, with a p-value of 2.04×10^{-7}. As this model component is used to produce the emission spectrum of a hot diffuse gas or optically thin plasma, this fits the picture of an ADC source, as concluded by P. Hakala et al. (2005).

We also noted small residuals remaining in the model fit, including a feature near 0.57 keV (or 21.7 Å), which we could fit with an additional narrow Gaussian with a significance of 3.7σ which could be the O VII He α-like emission line, which is not fitted by the MEKAL model component. However, it could not be identified in the RGS spectrum described below. Therefore, we did not include it in our final model for the EPIC-pn spectrum.

Table 2. The parameters of the continuum model for the 0.2–10 keV *XMM–Newton* EPIC-pn data. We indicate the 1σ uncertainties for each parameter.

Component	Parameter (Unit)	Value
TBABS	nH (10^{21} atoms cm^{-2})	1.04±0.03
BB	kT (10^{-2} keV)	7.2±0.3
	Norm (10^{-5})	1.3±0.2
PL	α	1.751±0.008
	Norm (10^{-3})	1.560±0.015
MEKAL	T (keV)	1.14±0.04
	Norm (10^{-4})	1.08±0.12
GAUSS	E_l (keV)	6.76±0.03
	σ (keV)	0.25±0.03
	Norm (10^{-5} photons cm^{-2} s^{-1})	1.7±0.15

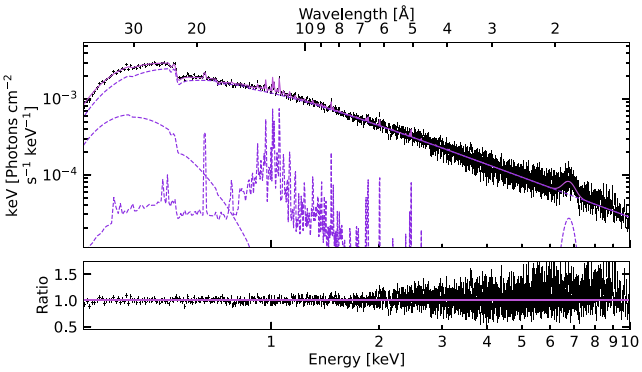

Figure 2. The time-averaged 0.2–10 keV X-ray spectrum of UW CrB, recorded using *XMM−Newton* EPIC-pn. In the upper panel, we show the spectrum with the y-axis in log space, and the data have been visually rebinned (5σ and at least 20 counts per bin) for clarification. The full model is shown using the solid line, and the model components are shown using dashed lines. In the lower panel, we show the ratio of the model and the data.

Using this model, TBABS X (BB + PL+ MEKAL + GAUSS), we obtain an adequate fit with a χ^2 value of 2199.28 with 1951 dofs, or a χ^2_ν of 1.13. The parameter values are shown in Table 2, and we show the full EPIC-pn spectrum and model fit in Fig. 2. The total model flux is $f_X=(1.22^{+0.017}_{-0.016})\times10^{-11}$ erg cm^{-2} s^{-1}, corresponding to a luminosity of $L_X\approx(5.26\pm0.07)\times10^{34}(\frac{d}{6\mathrm{kpc}})^2$ erg s^{-1}.

3.1.2 RGS

For the RGS 1 and 2 data, we attempt to fit both spectra with an absorbed black body model, as the data only covers energies <2 keV (see Section 2.1). From this fit, we clearly note residuals in the spectrum. We note a strong emission feature around 24.8 Å, corresponding to the N VII line. The significance of this line is 4.6σ. This agrees with the findings in S. Fijma et al. (2023) and our findings in Section 3.2, that the N V 1240 Å emission line is the strongest emission line in the FUV spectrum. The nitrogen enhancement is, in turn, likely due to the CNO-processed material from the companion star/accretion disc. The width of the emission line when fitting the line over the wavelength range presented in the inset of Fig. 3 is $\sigma=1400^{+400}_{-500}$ km s^{-1}, which corresponds to a full width at half maximum (FWHM) of 3300^{+900}_{-1200} km s^{-1}. We find that the central line wavelength is 24.79 ± 0.02 Å, meaning that the line is consistent with being at the rest wavelength. The line is not detected in the EPIC-

[4] https://www.swift.ac.uk/user_objects/index.php
[5] https://www.swift.ac.uk/analysis/uvot/

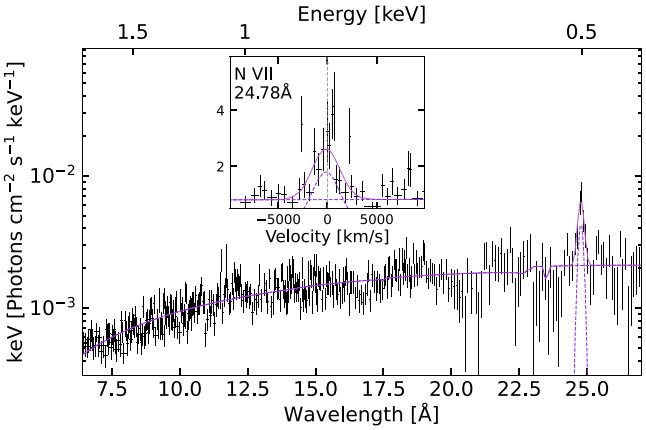

Figure 3. The time-averaged *XMM–Newton* RGS first order X-ray spectrum, shown between 6.4 and 27 Å (0.46–1.94 keV), and the data have been visually rebinned (3σ and at least 20 counts per bin) for clarification. We show the detected N VII 24.78 Å line in an inset in velocity space, where 0 km s^{-1} indicates the line rest wavelength.

pn spectrum, likely due to the limited spectral resolution around 24.8 Å/0.5 keV. We use the full model TBABS X (DISKBB + GAUSS) for the first order RGS spectrum, which we show in Fig. 3. This provides a goodness-of-fit of 2230 C-stat for 2020 dof, or a 1.10 reduced C-stat.

3.2 The UV spectrum

In Fig. 4, we show the combined spectrum of each visit, with the note that this will smear out shifts or changes as a result of the orbital phase, as each visit covers around $\approx 0.8\phi$ in total of the orbital phase of UW CrB. Similar to S. Fijma et al. (2023), we find a strong N V 1240 Å doublet emission line, and we clearly detect O IV 1343 Å, O V 1371 Å, the Si IV 1400 Å doublet, and He II 1640 Å. Moreover, we detect the N IV 1719 Å line.

We also detect a faint emission line near C IV 1549 Å in the visit 3 spectrum. S. Fijma et al. (2023) only found hints of the C IV emission line in archival HST data, with only two exposures in the wavelength range covering C IV. The detection of C IV allows for further constraints on the composition of the companion star and accreted material. The relative strength of the N V line compared to the strength of the C IV emission line suggests that the material is strongly CNO-processed (e.g. C. A. Haswell et al. 2002; C. S. Froning et al. 2011; N. Castro Segura et al. 2024; M. Georganti et al. 2025). The line ratios, and thereby the degree of CNO-processing, suggests that UW CrB's companion is the CNO-core of a more massive (1.3−2 $M_\odot$) stripped companion star (cf. N. Castro Segura et al. 2024). Exploring the evolutionary status of the companion star, as well as the evolutionary history of the binary, will be explored in a separate work.

As can be seen in Fig. 4, we do not identify P-Cygni features as in S. Fijma et al. (2023). However, we do identify substantially broadened features, which could be tracing an outflow. We expand on this in Sections 4.3 and 5.

3.3 The optical spectrum

For the optical spectrum of UW CrB, we have data sets from two telescopes: GTC and VLT. We show the time-averaged normalized spectra for the GTC/R2500R grism (5580−7690 Å) in Fig. 5, for the GTC/R1000B grism (3630–7000 Å; single exposure) in Fig. 6, and for VLT/XShooter (3000–24800 Å) in Fig. 7. Due to low SNR and the high amount of noise in the NIR arm, we leave the wavelength range from 11 000−24 800 Å out of the analysis.

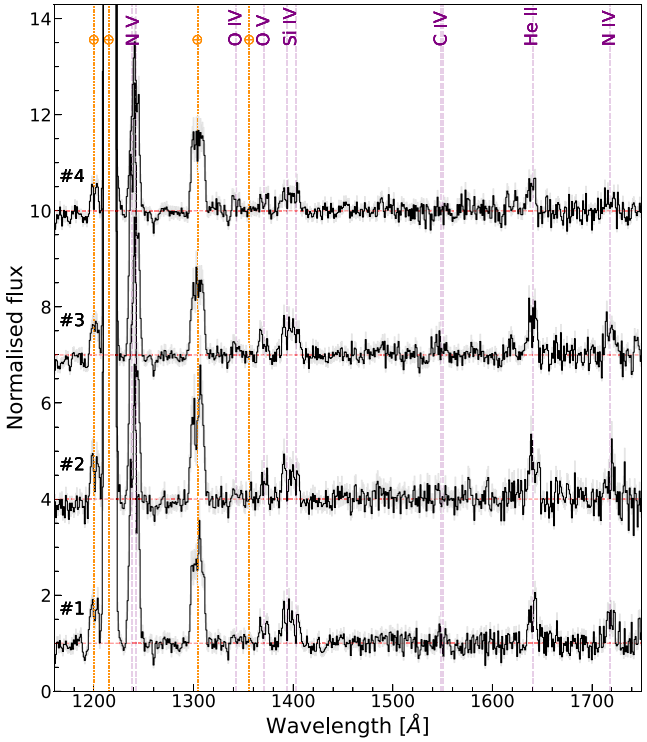

Figure 4. The normalized, time-averaged FUV spectra of UW CrB. We show the combined spectra of each *HST* visit separated by a vertical offset of 3 per visit, and rebin the spectra to 1 Å per bin for clarity. We show the identified lines using dashed lines. Terrestrial airglow emission features are marked with orange lines and plusses. Unlabelled narrow absorption features are interstellar.

3.3.1 GTC

The typical line profiles produced by a rotating accretion disc in an LMXB are either double-peaked or single-peaked emission lines (e.g. K. Horne & T. R. Marsh 1986). For the GTC/R2500R spectrum (Fig. 5), we find double-peaked emission for the H α line, as well as a deep and broad absorption profile. To check if the emission feature could be associated with a traditional double-peaked profile from a rotating accretion disc, we compare the separation between the two emission peaks ($\Delta v_{\rm peak}$) for H α to the peak-to-peak separation for other lines. We identified the peaks of the double-peaked line by visual inspection and fit each of them with a Gaussian profile. We find $\Delta v_{\rm peak}$ is around $\approx$900 km s^{-1} in velocity space for H α, which is consistent with $\Delta v_{\rm peak}$ for He II 1640 Å and He II 4686 Å in the *HST* and VLT spectra, respectively (both around $\approx$800 km s^{-1}). Notably, we find that the blue emission peak appears much stronger than the red emission peak for H α in the GTC/R2500R spectrum.

We also detect some single-peaked emission lines in the GTC/R2500R spectrum. For He I 5876 Å, we find an emission peak in a broad, deep absorption profile, and for He I 6678 Å, we note a faint emission line as well. In both of the aforementioned lines, the emission appears slightly blue-shifted with a velocity of around −700 to −600 km s^{-1} when fitting each respective line with a single

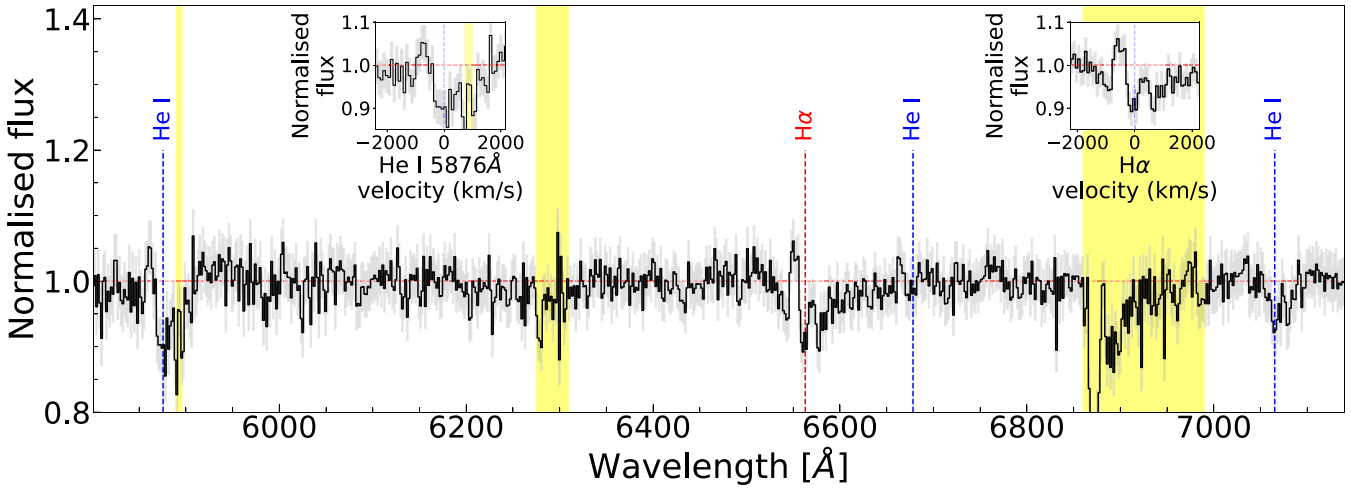

Figure 5. The normalized time-averaged optical spectrum of UW CrB as recorded using GTC/OSIRIS with the R2500R grism. We rebin the spectrum to 1.75 Å per bin for clarity, and indicate the identified lines using dashed lines. The yellow highlighted regions indicate telluric absorption. We also show insets of the He I 5876 Å and Hα lines in velocity space, where 0 km s^{-1} is the rest wavelength for the respective line.

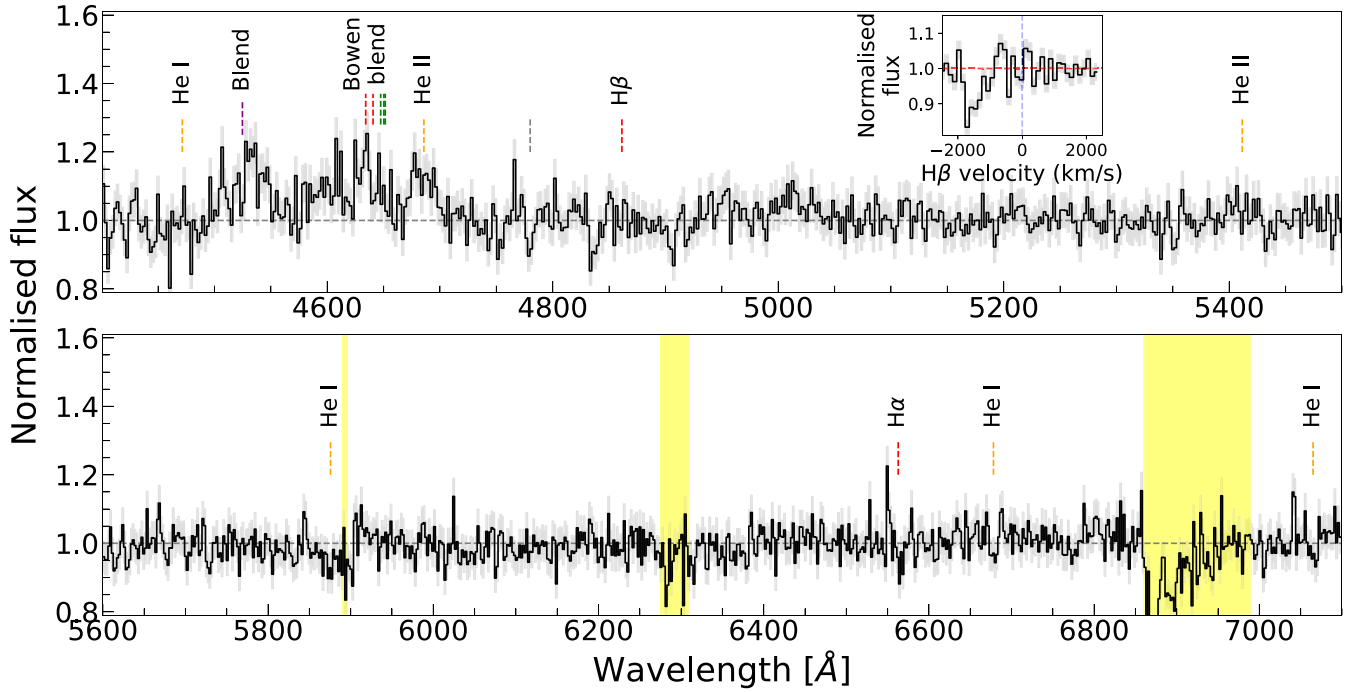

Figure 6. The normalized time-averaged optical spectrum of UW CrB as recorded using GTC/OSIRIS with the R1000B grism. We indicate the identified lines using dashed vertical lines. The (grey) dashed vertical line indicates a potential diffuse interstellar band (DIB) at 4780 Å. We also show an inset of the H β line in velocity space, where 0 km s^{-1} is its rest wavelength. The highlighted regions indicate telluric absorption.

Gaussian. As this is similar to the velocity of the stronger blue peak in the H α line, the blue-shifted emission for He I 5876 Å and 6678 Å lines appear consistent with the stronger blue peak of the line profile.

We also note deep and broad absorption profiles for some lines. For H α, the blue and red edge of the absorption component reach to -1500 and 1550 km s^{-1} when compared to the continuum, respectively. For He I 5876 Å, the blue and red edge of the absorption reach to -2300 and 1600 km s^{-1}, respectively. Finally, for the He I 7065 Å line we only note an absorption feature around the rest velocity. The broad absorption and strong blue emission peaks for the H α and He I 5876 Å are even more apparent in the individual exposures and show changes on short ($\approx$20 min) time-scales, which we discuss in Section 4.4.

Finally, for the GTC/R1000B spectrum (Fig. 6), we note some additional lines, such as He II 5411 Å and the Bowen blend at around 4643 Å. We also note a He II 4686 Å emission line, which appears double peaked with a slightly stronger blue emission peak. Notably, there appears a clear blue-shifted absorption profile and a faint double peaked emission around H β as identified through visual inspection.

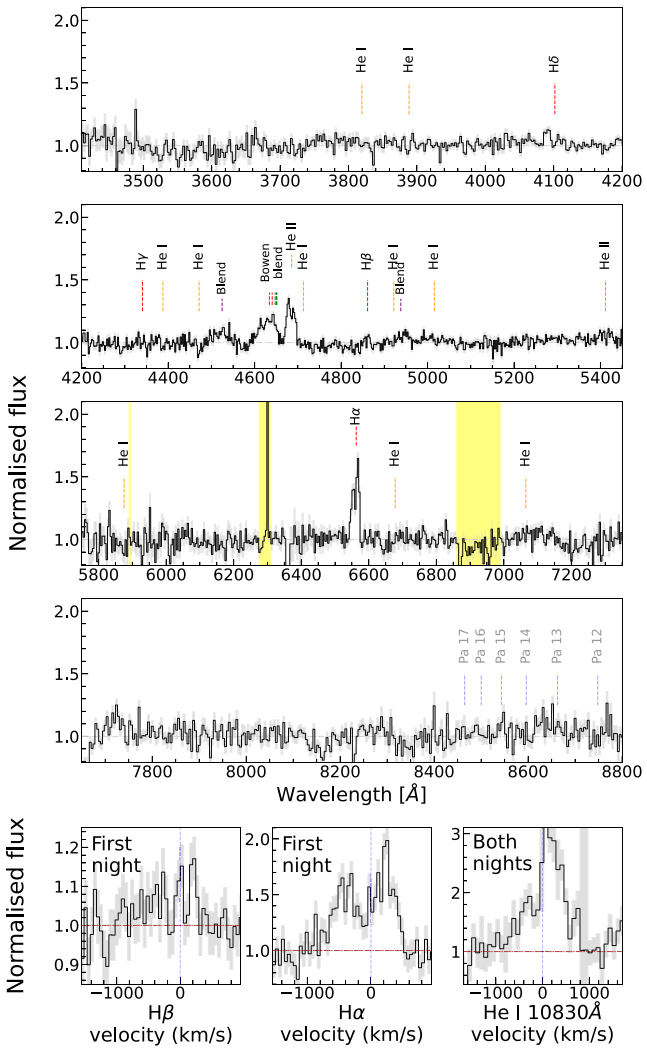

Figure 7. The normalized time-averaged optical spectrum of UW CrB as recorded using VLT/XShooter. We indicate the identified lines using dashed vertical lines, and indicate typical LMXB lines with faint blue dashed lines. We rebin the time-averaged spectrum to 0.25, 0.4, and 0.3 Å, for the UVB, VIS, and NIR spectra, respectively. Moreover, we show panels for the H α, H β, and He I 10 830 Å lines in velocity space in the first, second and third panel on the bottom, respectively. We show H α and H β for the data set for the first night, and He I 10 830 Å for the time-averaged profile over both nights. For all three panels, 0 km s^{-1} indicates the rest wavelength for the respective line.

The emission line is tentatively identified, but appears double peaked. This is similar to the H β line as identified in the VLT data, which will be described in the next section. We do not note a broad absorption as we identify for H α, and we do not detect an absorption component redward of the line. Therefore, the line profile for H β appears to trace an outflow. The significance of the blue-shifted absorption component for H β is 7.3σ, when comparing this to the continuum SNR around the line of 43.6. The blue edge of the absorption profile extends to around -1800 km s^{-1}, indicating the terminal velocity of the potential outflow. The exposure was recorded during phases $\phi = 0.67-0.82$, which is consistent with the UV outflow recorded in S. Fijma et al. (2023). In order to study this wavelength range further, we use the VLT data.

3.3.2 VLT

For the combined VLT/XShooter spectrum (recorded over 2 nights and 6 h total; Fig. 7), we detect several emission and absorption lines. We also note clear asymmetries in some lines.

Both the He II 4686 Å and H δ emission lines show distinct double peaked emission with a stronger blue peak, similar to the line profiles detected in the GTC spectrum recorded 5 d earlier. However, this is not the case for H α and H β. Both H α and H β are double peaked, but show stronger red emission peaks. Moreover, for H α the deep, broad absorption detected in the GTC spectrum is no longer evident. Furthermore, we note that the strong He I 10830 Å emission line, which we show in an inset, also appears asymmetric and red-skewed.

We also note a hint of blue-shifted absorption for H β, with a blue-edge velocity of -1300 km s^{-1}. In the time-averaged line profile over both nights, when comparing the absorption feature to the SNR of the nearby continuum, the component only has a significance of 2.1σ, so we consider this as a tentative absorption feature. On the first night, both H β and H α appear to show tentative blue-shifted absorption, as shown in Fig. 7. However, these only have significances 2.1σ and 1.2σ for H β and H α, respectively.

Other emission lines are detected that show no obvious asymmetries, such as a faint double peaked He II 5411 Å emission line, and a faint double peaked Hγ line. Furthermore, we note broad emission features at 4525 Å, 4643 Å, and 4938 Å. The broad emission feature at 4643 Å is the Bowen blend. This line appears slightly asymmetric or blue-skewed considering the rest wavelengths of the N III (4634 Å, 4640 Å) and C III (4647 Å, 4650 Å, 4651 Å) transitions attributed to the Bowen blend. However, this could potentially be related to the the lower abundance of carbon and higher abundance of nitrogen, as derived for the UV spectrum in Section 3.2. This would also be consistent with the broad emission at 4525 Å, which contains N III transitions (4510 Å, 4515 Å).

Finally, we can compare our findings with S. L. Morris et al. (1990), who note that some He I absorption lines appeared blue-shifted in their optical spectra. We detect several He I lines in the spectrum, with some in absorption, including He I 3889 Å, 4388 Å, 4471 Å, and 4922 Å. We found that some He I lines appeared slightly blue-shifted by around -133 km s^{-1}. However, when comparing this shift to double-peaked emission features such as H α, H β, H δ, we find that their line centres are shifted to the same degree. Therefore, we suggest that this slight blue-shift of -133 km s^{-1} could be related to the systemic velocity of the system. This is supported by the interstellar Ca II 3934 Å and 3948 Å absorption lines being recorded at rest. Potentially, the system got a natal kick in its formation, which is also in line with its location above the Galactic Plane.

4 TIME-RESOLVED ANALYSIS

4.1 Time-resolved photometry

In order to study phase-resolved and time-resolved information on UW CrB, we start by analysing the light curves. We show the full *XMM–Newton* X-ray and *HST* FUV light curves of Epoch 1 and 2 in Fig. 8. For all the time-resolved analysis in this section, we determine the orbital phase using the ephemeris of M. R. Kennedy et al. (2024).

4.1.1 X-ray light curve

The total X-ray light curve covers around 17 source orbits (P_{orb}=110.98 min), and around 25 per cent of the 'recurrence' period or disc precession period ($P_{prec}\approx$5.5 d). The light curve shows

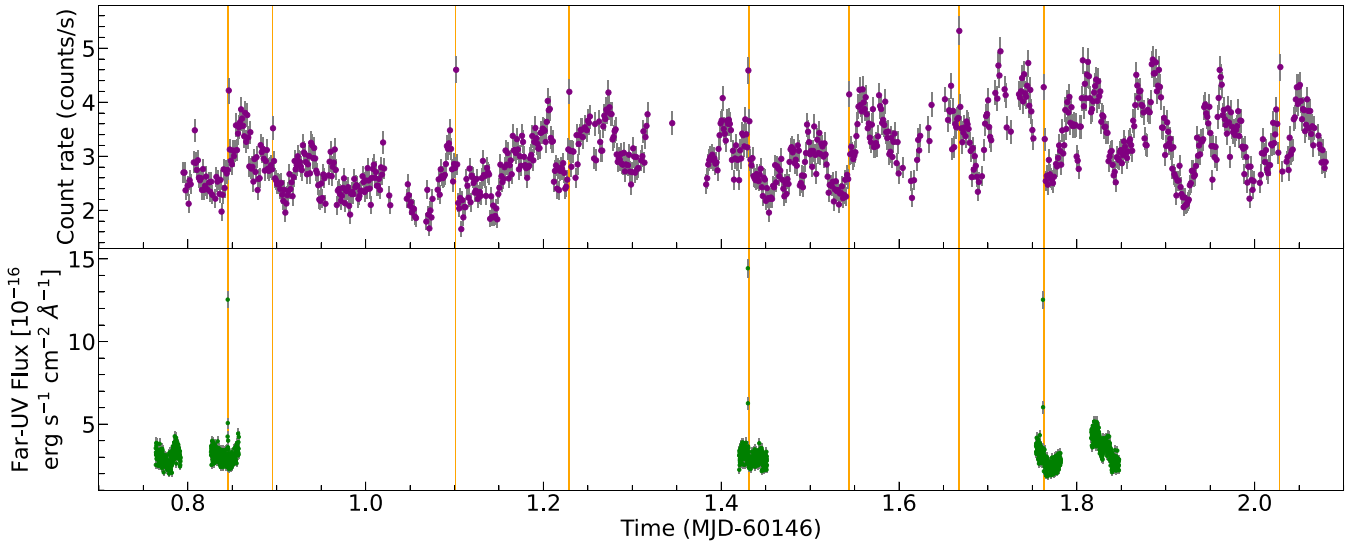

Figure 8. The X-ray and FUV light curves from Epoch 1, recorded using the *XMM–Newton* and *HST* telescopes, respectively. In the top panel, we show the X-ray light curve binned to 100 s bins. In the bottom panel, we show the UV light curve binned to 10 s bins. We show type-I bursts identified using the 5 s binned *XMM–Newton* light curve using vertical lines. We find that three type-I bursts are recorded simultaneously with both telescopes.

several forms of variations. Firstly, *XMM–Newton* recorded several type-I bursts, as indicated in Fig. 8. As we only sample 121 ks, and as some of the light curve is masked because of background flaring, we cannot fully constrain the burst rate of UW CrB. Keeping this in mind, in Epoch 1, we record a type-I burst roughly every 4 h. Comparing this to previous work, P. A. Mason et al. (2012) conclude that there is no constant burst rate for UW CrB. They found that the mean interval between bursts varied between 55 min between bursts to no bursts being recorded in six successive nights, with no correlation found between the burst rate and mean optical brightness of UW CrB for example.

Secondly, we note broad modulations in the light curves. We show the phase-stacked light curves in Fig. 9. There is a modulation spanning around 50 to 70 per cent of the orbital phase and with a minimum at approximately $\approx 0.5-0.7\phi$, that is more shallow at the start of the exposure, and becomes more wide and deep at the end. The shape and depth of these modulations are consistent with those reported in P. Hakala et al. (2005). During either of these modulations, the X-ray flux never reaches zero, indicating that nothing fully eclipses the X-ray reprocessing/scattering region. Furthermore, the deepest point of the eclipse appears to slightly change in phase over time, from around 0.55ϕ to 0.75ϕ in the orbits where the deepest point can clearly be identified. As suggested by previous works, these modulations appear to be the result of an out of plane structure, unlike the modulations measured in the optical band (as presented in e.g. P. Hakala et al. 2005; P. A. Mason et al. 2012). The changing modulations, in turn, have a recurrence period of 5.5 d (e.g. P. A. Mason et al. 2008, 2012; P. Hakala et al. 2009).

There are also sometimes more shallow and narrow dips with a minimum at approximately ≈ 0.1–0.15ϕ, and spanning around 20 to 30 per cent of the orbital phase. This is notable in orbits #1, #6, #9, #10, #13, #14, #15, #15, #16, and #17 in Fig. 10. Finally, we note some smaller and more random variations in the phase-stacked light curves as well, as also reported in P. A. Mason et al. (2008, 2012). We are unsure about the exact origin, as it could be related to the superhump-like variations, accretion variability, geometry, and/or the accretion stream.

We have two *Swift/XRT* observations during Epochs 1 and 2, which we can use to compare the X-ray behaviour during the two Epochs. We calculate the flux by fitting the *XRT* spectra between 0.7–10 keV using an absorbed power-law (TBABS X POWERLAW) continuum model (e.g. R. Wijnands et al. 2015). We find that the X-ray flux is $(7.6\pm0.7)\times10^{-12}$ erg cm^{-2} s^{-1} during Epoch 1, and $(0.81\pm0.2)\times10^{-12}$ erg cm^{-2} s^{-1} during Epoch 2. We also include this in Table 3. When binning the light curves for these exposures to 100 s bins, we note similar modulations as are recorded for the *XMM–Newton* light curves. Despite the modulations, the X-ray flux appears overall higher in Epoch 1 than in Epoch 2.

4.1.2 *UV light curve*

For the UV emission, *HST* recorded 3 visits simultaneously with *XMM–Newton*. Three type-I bursts were recorded simultaneously and detected in the UV light curve as well. When comparing the average FUV flux from these exposures (i.e. around $f_{\rm uv}\simeq 3\times10^{-16}$ erg s^{-1} cm^{-2} Å^{-1}) to those in S. Fijma et al. (2023) (i.e. around $f_{\rm uv}\simeq 8\times10^{-16}$ erg s^{-1} cm^{-2} Å^{-1}), the emission is half the brightness of 2012 archival *HST* data.

The shape of the light curves has changed as compared to S. Fijma et al. (2023) as well. This is most apparent when phase-folding as shown in Fig. 10. This also includes visit 4 recorded in Epoch 3. In this plot, we show that we cover almost all parts of the orbital phase as well. As in the X-ray light curves, we see a wide modulation in the UV light curve as well, spanning around half of the orbital phase. The modulations are relatively shallow, and never fully eclipse the UV emission. However, we currently do not have enough information to determine what causes the modulations, as we do not have UV light curves over the full precession phase.

From the *Swift/UVOT* exposures, we derive the optical and UV flux densities during Epochs 1 and 2 in order to compare the UV flux behaviour. We show the results of extracting the fluxes in Table 3. We find that, like the X-ray flux, the Epoch 2 flux is substantially lower than the Epoch 1 flux, with the exception of the flux density measured in the *b* filter. The variations in optical and UV flux density

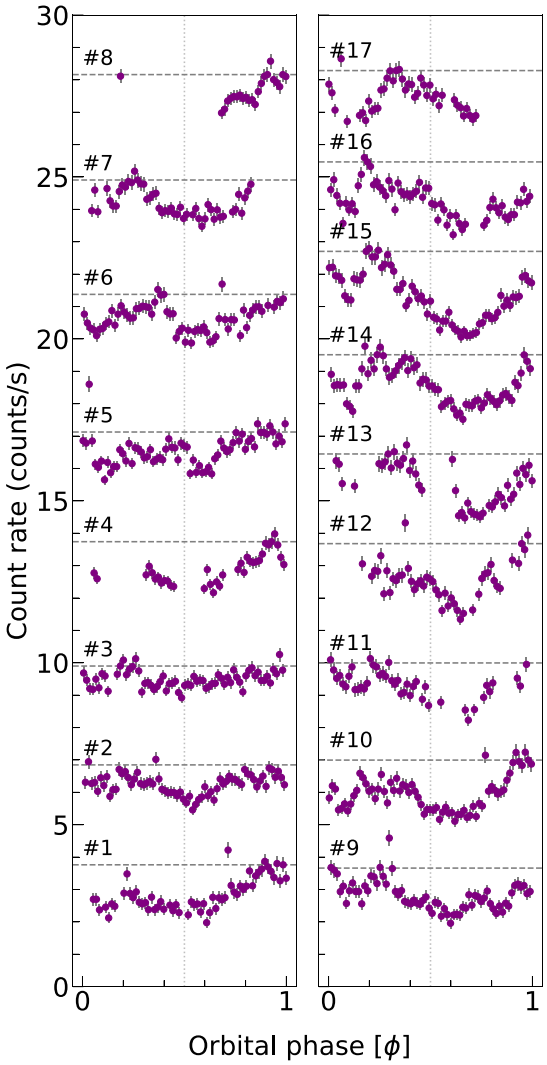

Figure 9. The X-ray light curves per binary orbit, shown using 100 s time bins. 17 recorded binary orbits are plotted with a vertical offset in two panels. The orbits are plotted consecutively and numbered according to their order in time. Each light curve is offset with 3 counts/s per orbit from #1 and #9 onward. Phase ϕ=0 indicates the phase where the companion eclipses the compact object. We indicate the maximum of the rolling average (calculated per 3 bins) per orbit using a grey horizontal dashed line, in order to indicate the approximate non-obscured continuum flux per orbit. We indicate phase 0.5 with a vertical grey dotted line for clarity.

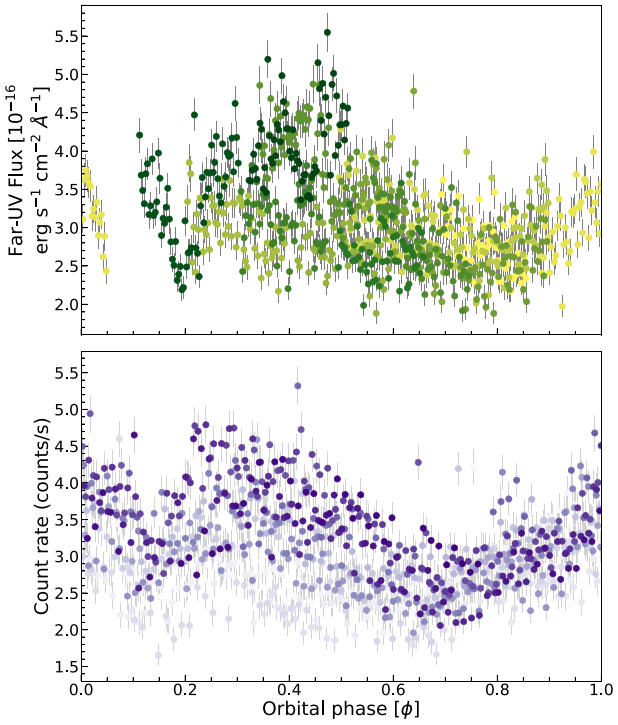

Figure 10. The FUV and X-ray light curve folded in orbital phase. Phase ϕ=0 indicates the phase where the companion eclipses the compact object. We crop out the peaks of all type-I bursts. In the top panel, we show the UV light curve binned to 20 s bins, and plotted using a sequential colourmap. We also include the data from visit 4 recorded in Epoch 3. In the bottom panel, we show the X-ray light curve binned to 100 s bins and plotted using a sequential colourmap. We note a broad modulation spanning more than half of the orbital phase.

Table 3. The unabsorbed X-ray flux and UV flux density, obtained using the *Swift XRT* and *UVOT* observations in Epoch 1 and 2.

XRT		Epoch 1 flux (10^{-12} erg cm^{-2} s^{-1})	Epoch 2 flux (10^{-12} erg cm^{-2} s^{-1})
		7.6 ± 0.7	0.81 ± 0.2
UVOT	Filter	Epoch 1 flux density (10^{-16} erg cm^{-2} s^{-1} Å^{-1})	Epoch 2 flux density (10^{-16} erg cm^{-2} s^{-1} Å^{-1})
	uvw2	3.02 ± 0.19	1.39 ± 0.13
	uvm2	2.47 ± 0.25	1.53 ± 0.18
	uvw1	2.53 ± 0.2	1.08 ± 0.15
	u	1.73 ± 0.17	0.79 ± 0.14
	b	0.83 ± 0.17	0.85 ± 0.16
	v	<0.64	<0.63

appear consistent with the variations in the flux density measured in the FUV (S. Fijma et al. 2023).

4.1.3 *Ruling out a near* L_{EDD} *accretion rate*

In order to study if and how disc wind outflows can be launched in UW CrB, a constraint on the accretion rate is required. As UW CrB is proposed to be an ADC source, and the X-ray emission is obscured and scattered into our line of sight, we cannot fully constrain the accretion rate using the X-ray data. Based on the orbital period and measured optical brightness (e.g. J. Paradijs & J. E. McClintock 1994), the accretion rate is proposed to be $L_X \approx 1$–10 per cent L_{EDD}, which is consistent with amplitude, burst recurrence, and duration of the detected type-I bursts. However, this does not fully exclude that the source is accreting at a much higher rate (around L_{EDD}; also known as Z-sources in the literature), as this could also result in frequent bursts (e.g. M. Sztajno et al. 1986; E. Kuulkers, M. van der Klis & J. van Paradijs 1995; A. P. Smale 1998; E. Kuulkers et al. 2002; M. Linares et al. 2010). In this case, the source would show bright ($\approx$mJy) radio emission with strong variations on day time-scales (as shown for Z-sources at a similar distance, such as GX 17+2 at $\approx$8 kpc; e.g. W. Penninx et al. 1988). Therefore, we recorded the radio emission every day for 2 weeks. Moreover, in order to study the (quasi-)simultaneous X-ray behaviour, we monitored with *Swift* as well. Over Epoch 3, we detect no radio emission from UW CrB. The

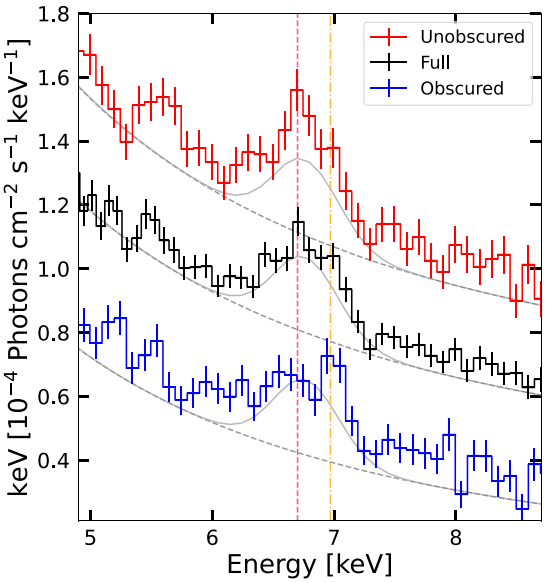

Figure 11. The Fe Kα region in the flux-resolved *XMM–Newton* EPIC-pn spectra. We show the full time-averaged spectrum in the middle of the figure, the unobscured data set at the top and the obscured data set at the bottom of the figure. The spectra have been visually rebinned (20σ and at least 20 counts per bin), and we added a vertical offset of 0.25×10^{-4} to the full data set and 0.5×10^{-4} to the unobscured data for clarity. We add a vertical dashed and a dash–dotted line to indicate the 6.7 and 6.97 keV lines, respectively. We show the model for the EPIC-pn spectrum using a solid line, where we fit a single Gaussian model to the Fe Kα line for the full data set, and tie the parameters of this Gaussian to the single Gaussian models fitting the line in the unobscured and obscured data set.

recorded RMS (root mean square) noise values range between 44 and 783 μJy for the individual observations. Based on our sampling and non-detections with AMI-LA, we can rule out a near L_{EDD} accretion rate for UW CrB.

We obtain a 3σ upper limit of 120 μJy when combining all observations. Assuming a distance of around 6 kpc, we derive an upper limit for the radio luminosity of around $L_R < 8 \times 10^{28}$ erg s^{-1} at 15.5 GHz. When comparing this to other NS-LMXBs, we find that we cannot use this upper limit to constrain the spectral state of UW CrB, as both hard- and soft-state NS-LMXBs have been detected at higher and lower radio luminosities (e.g. J. den Eijnden et al. 2021).

4.2 A changing Fe–K α profile in the X-ray spectrum

Using our *XMM–Newton* data, we attempt to perform time-resolved spectroscopy, but this is constrained by the low count rate of the data. Therefore, we create a spectrum of all data where the X-ray flux is lower than 3 cts s^{-1}, i.e. when the X-ray emission is being obscured and we see a modulation in the light curve (the 'obscured' data set), and a spectrum of all data where the X-ray flux exceeds 3 cts s^{-1}, i.e. where the X-ray flux is not obscured (the 'unobscured' data set).

Other than small changes in the normalization, temperature of the black body, and power-law index, the most striking change is observed in the Fe Kα line. We show the Fe Kα line for the full spectrum and the flux resolved spectra in Fig. 11. From this figure, we find that the line looks quite different in the 'obscured' spectrum, than in the other two spectra. There appear to be two line components in the spectrum; one broad, potentially red-skewed and asymmetric Gaussian with a central energy of 6.6 keV, and a narrow Gaussian with a central energy of 7 keV. These appear to represent a broad, red-skewed Fe XXV 6.7 keV line, and a narrow, slightly blue-shifted Fe XXVI 6.97 keV line.

We test the presence of two line components by fitting two Gaussians, and show the results in Table 4. This seems to suggest that the Fe XXV 6.7 keV line becomes flatter, wider and slightly red-skewed during the X-ray modulations. When determining the significance of the two line components, we find 2.98σ and 2.89σ for the broad and narrow Gaussian, respectively, meaning that the two line components cannot be significantly identified. We discuss the line and the changing profile in Section 5.

4.3 A broadened Si IV line in the UV data

We also perform time-resolved spectroscopy of the UV data. Our goal is to check if we can find P-Cygni features like those reported in S. Fijma et al. (2023) for the Si IV 1400 Å and N V 1240 Å lines. From the individual exposures, we do not find significant blue-shifted absorption or P-Cygni profiles for these lines.

We do note that the Si IV emission line appears much broader than those detected (close in time to) the identified P-Cygni profiles in S. Fijma et al. (2023). Line broadening has been attributed to accretion disc winds in previous UV and optical studies (e.g. A. J. Bayless et al. 2010; F. Rahoui et al. 2014), also especially after detection of P-Cygni outflow features (e.g. T. Muñoz-Darias et al. 2016). A. J. Bayless et al. (2010) find evidence for a high velocity wind from the C IV doublet line for the ADC source X1822−371, and derive the projected velocities from the full width at zero intensity (FWZI) of this line. Therefore, we initially attempt to study the Si IV emission line width by measuring the FWZI. We measure this in all individual sub-exposures by modelling the normalized line doublet with a double Gaussian model. We measure the boundaries where the double Gaussian model deviates 0.005 from the normalized continuum as an approximation, and use the difference between those boundaries in wavelength to estimate the FWZI. Moreover, we check if this consistent with a deviation from the measured continuum in all spectra.

We find that the FWZI of the Si IV doublet in the archival data is around 16 Å in the exposure directly preceding the outflow detection, and in the exposure where the outflow is detected in S. Fijma et al. (2023). In all other exposures, the FWZI is on average around 35 Å. The FWZI of 35 Å corresponds to a projected velocity of around 3750 km s^{-1}. As we have previously detected P-Cygni features for Si IV, we could associate the detection of broad line profiles for this line to the material expanding at the outflow velocity and becoming optically thin, as was suggested for some UV emission lines in X1822−371, and as typically observed in expanding nova shells (e.g. J. G. Cohen & A. J. Rosenthal 1983; C. D. Gill & T. J. O'Brien 1999).

However, the actual broadening of the line is complicated to assess, as the line consists of two atomic transitions, at 1394 Å and 1403 Å. We note that in some individual *HST* sub-exposures, the line profile appears to show double peaked emission features for both transitions, similar to the median line profile shown in Fig. 12. In other sub-exposures, the profile appears to show single peaked emission lines for both transitions, also showing asymmetries in the line strength and shape, but still showing broad line profiles with FWZIs between 25 and 30 Å. This means that fitting the line and constraining the line width consistently is challenging. This is further complicated by the lack of uncertainties based on this estimation of the FWZI.

Table 4. Fits to Fe K α line in flux-resolved spectra. The 1σ uncertainty on the normalization on the two Gaussian components are calculated with the width of the other Gaussian component fixed. For the width of the second Gaussian for the obscured data set, the 1σ uncertainty of the width cannot be constrained, likely due to the limited resolution of the EPIC-pn instrument and the narrowness of the line.

Data set	Model	E_0 (keV)	σ (keV)	Norm (10^{-5} phot cm^{-2} s^{-1})
Full	1 gauss	6.76±0.03	0.25±0.03	$1.7^{+0.16}_{-0.15}$
Unobscured	1 gauss	6.75±0.03	0.23±0.04	1.8±0.2
Obscured	1 gauss	6.81±0.07	0.28±0.06	1.2±0.2
	2 gauss	6.57±0.11	0.27±0.10	0.8±0.2
		7.01±0.02	0.038	$0.53^{+0.16}_{-0.14}$

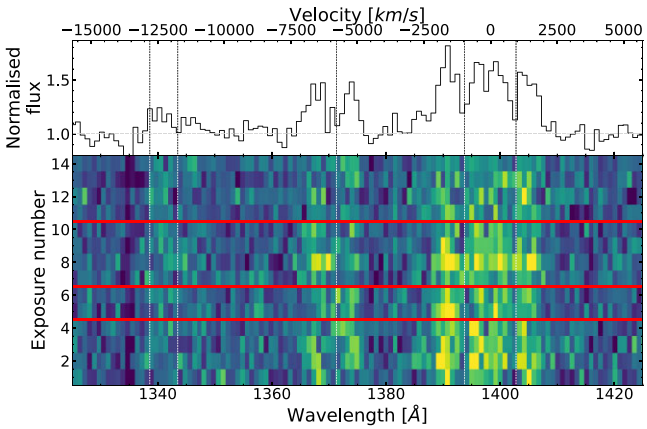

Figure 12. The Si IV 1400 Å, O IV 1343 Å, and O V 1371 Å lines. We show the normalized median line profile in the top panel, and the trailed spectrum in the bottom panel. The bottom x-axis shows the wavelength in Å, and the top x-axis we show the velocity relative to the rest wavelength of the Si IV 1400 Å line. On the y-axis we show the exposure number, and separate each visit with a horizontal line. We indicate the rest wavelength of each line using vertical dash–dotted lines. We note that the narrow absorption blue-ward of the O V 1343 Å line is interstellar.

Moreover, the FWZI metric is also sensitive to SNR and resolving power. Therefore, we ultimately cannot draw strong conclusions from the FWZI of Si IV alone.

We do note that the scenario where the Si IV emission line is formed in an optically thin (expanding) material, is further supported by the line never being eclipsed in the FUV data, despite the observations both covering a broad modulation in the UV flux (similar to the X-ray data), and despite the data covering phase ϕ=0, as shown in Fig. 10. This is evident from the trailed spectra of the Si IV 1400 Å line, which we show in Fig. 12. We also explicitly by extracting time-resolved spectra during the eclipse (ϕ≈0.98–1.02) and find that the Si IV 1400 Å emission line, as well as N V 1240 Å, O V 1371 Å, He II 1640 Å, and N IV 1719 Å lines, are still clearly detected. This suggests (some) line emission is formed above the disc, potentially suggesting that Si IV could be formed in an (equatorial) outflow or disc wind.

4.4 Time-resolved optical spectroscopy

4.4.1 VLT

We show trailed spectra for the first observing night of the H α line in Fig. 13, and for the He II 4686 Å line in Fig. 14. As the data of the second night of observing was substantially noisier, we do not include these in the figures.

The trailed spectrum of He II 4686 Å shows that the emission line is never being eclipsed during the orbit, and especially the blue emission peak at a velocity of around -600 km s^{-1} remains strongly present over almost all exposures. Moreover, we find that the H α shows double peaked emission during the full orbital phase. In the left plot in Fig. 13, the emission appears reduced in flux during the eclipse of the companion around ϕ≈1, but less so during ϕ≈2. Due to the low SNR in the individual exposures around H α (around 1.2 on average), identifying emission around the eclipse is challenging. However, by rebinning the data to increase the SNR, it appears that the H α emission is not fully occulted during either eclipse. These findings are consistent with the findings of M. R. Kennedy et al. (2024) for UW CrB. They suggest that the emission is potentially created above the plane of the disc for the He II 4686 Å line as well as partially for the Hα line.

For He II 4686 Å, we note some potential blue-shifted absorption around ϕ≈1.25. In order to check if this could potentially trace P-Cygni profiles, we check the individual line profiles, and show the three almost consecutive exposures (T_{exp} = 260 s each, UVB arm) with hints of blue-shifted absorption in Fig. 15. As the SNR in the individual exposures is low, we test if the blue-shifted absorption is significant by taking the weighted average of the three exposures. We show this line profile in Fig. 15 as well. Finally, we rebin the three individual exposures and the combined exposure to 0.85 Å per bin to increase the SNR, similar to the trailed spectra. There appears to be a blue-shifted absorption feature extending to about -1400 km s^{-1} for the combined exposure. However, this feature has a significance of only 2.5σ, based on the SNR of 7.5 for the combined exposure. Therefore, we consider this as a tentative P-Cygni feature. If these are indeed P-Cygni profiles tracing an outflow, they are recorded in a different part orbital phase than the UV P-Cygni feature was detected in (ϕ = 0.7−0.8; S. Fijma et al. 2023), as well as the blue-shifted absorption in the Hβ line in the GTC/R1000B spectrum.

Due to the low SNR of the Hα and Hβ lines in the individual exposures (1.2 and 2.1 for the respective lines), we could not determine the presence of P-Cygni profiles. As the He II 4686 Å line is the strongest line in the UVB spectrum, and as the SNR is the highest in the UVB arm for the individual spectra overall, this could be the reason we only identify hints of P-Cygni profiles in the individual spectra here, and not in other weaker lines such as Hβ, nor in the H α line in the VIS spectra. Moreover, the He II 4686 Å is often contaminated by the nearby Bowen blend emission line, which makes the detection of blue-shifted absorption difficult to detect in this line. However, due to evident weaker C abundances for UW CrB, and thus potentially weaker C III Bowen blend emission near He II,

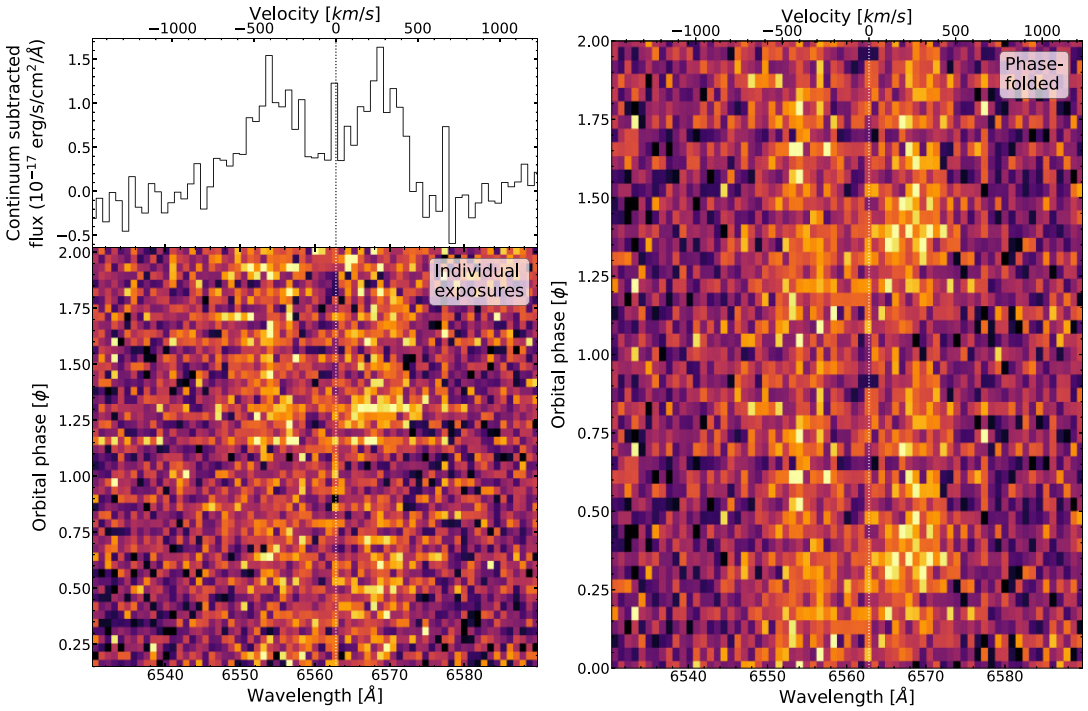

Figure 13. The trailed spectrum of the Hα line for the first night of VLT/XShooter observations. On the left figure, the trailed spectra for the individual exposures are shown. On the right figure, the phase-folded trailed spectra are shown, where we repeat the phase-folded spectra from phase 1 to 2. In the upper panel of the left figure, we show the median line profile of the line, where we have subtracted the underlying continuum. We show the rest line wavelength in both figures using a dotted vertical line. We plot the spectra with orbital phase on the y-axis. We rebin the spectra to 0.86 Å per bin to increase the SNR, and plot the colourmap between the 1st and 99th quantile for clarity.

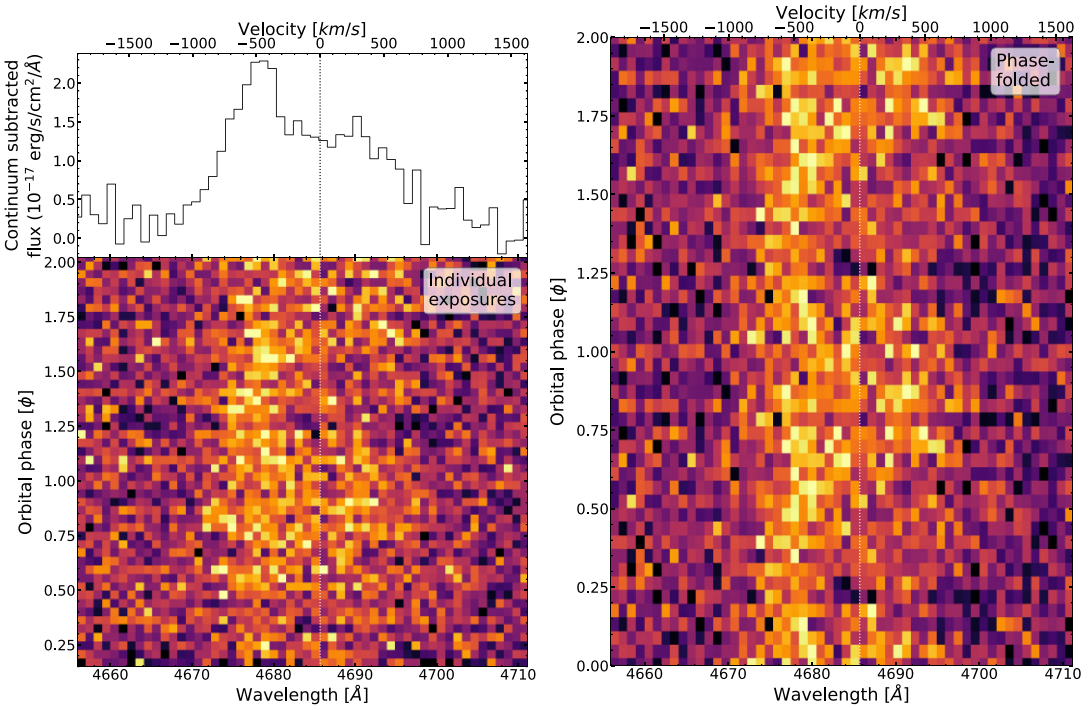

Figure 14. The trailed spectrum of the He II 4686 Å line for first night of VLT/XShooter observations. On the left figure, the trailed spectra for the individual exposures are shown. On the right figure, the phase-folded trailed spectra are shown, where we repeat the phase-folded spectra from phase 1 to 2. In the upper panel of the left figure, we show the median line profile of the line, where we have subtracted the underlying continuum. We show the rest line wavelength in both figures using a dotted vertical line. We rebin the spectra to 1 Å per bin to increase the SNR, and plot the colourmap between the 1st and 99th quantile for clarity.

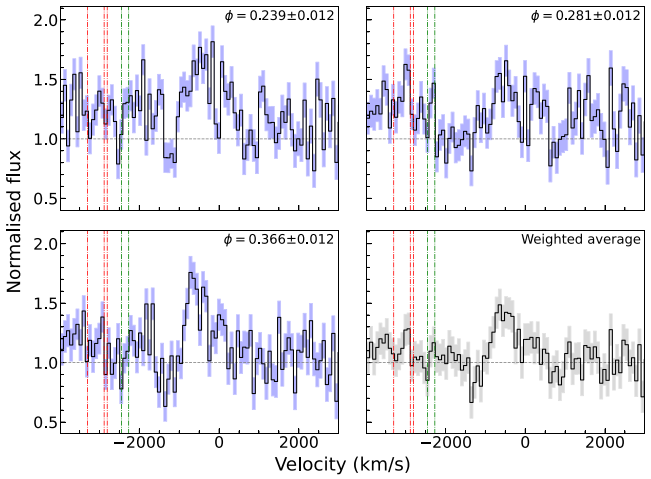

Figure 15. Tentative P-Cygni features found for the He II 4686 Å line in VLT data. We plot the normalized flux against the velocity at 4686 Å. We show the Bowen blend C III transitions at 4647 and 4650 Å in (green) dash-dotted lines, and the N III transitions at 4634, 4641 and 4642 Å in (red) dash–dotted lines. In the two upper panels and in the lower left panel we show the individual exposures where we identify potential absorption. We show the average orbital phase of the individual exposures in the upper right of each plot. In the lower right panel, we show the weighted average of the three exposures.

this might make the identification of blue-shifted absorption for He II more accessible. We discuss the outflow scenarios for UW CrB in more detail in Section 5.

4.4.2 GTC

For the individual GTC/R2500R spectra (≈1200 s), we see quite different changes in the line profile in time. We show the phase-folded, trailed spectra for the Hα, He I 5876 Å and 6678 Å in Fig. 16. We include the He I 6678 Å line because the emission line appears to be only present in some exposures.

For the Hα line, we noted a broad deep absorption component (spanning around 2500 km s^{-1}), a double peaked emission feature, and a stronger blue emission peak in the combined GTC spectrum. In the individual spectra, the broad absorption and blue emission peak are present in most exposures. Only in the two exposures around $\phi \approx 0/1$, we see an emission peak at around the rest velocity/wavelength, as well as shallow red-shifted absorption. For an individual exposure covering $\phi \approx 0/1$ specifically, we note a distinct double peaked emission feature. Detecting a emission peak around the rest wavelength when the companion eclipses the disc and compact object, further strengthens the interpretation that the Hα is partly formed above the disc. Potentially, a bi-conical wind could produce double peaked emission features in this case (e.g. J. H. Matthews et al. 2015; K. I. I. Koljonen et al. 2023).

For the He I 5876 Å line, we noted a broad absorption feature and only a blue emission peak in the combined GTC spectrum. In the individual spectra, this line profile is consistently present in most exposures. The absorption appears to be strongest around $\phi \approx 0.5$. In an individual exposure recorded at $\phi \approx 0.5$, we appear to only see absorption for He I, and the emission peak is completely suppressed. Similar broad absorption features have been suggested to be produced by optically thick regions in accretion discs of other LMXBs (e.g. G. Dubus et al. 2001). For the X-ray data recorded simultaneously

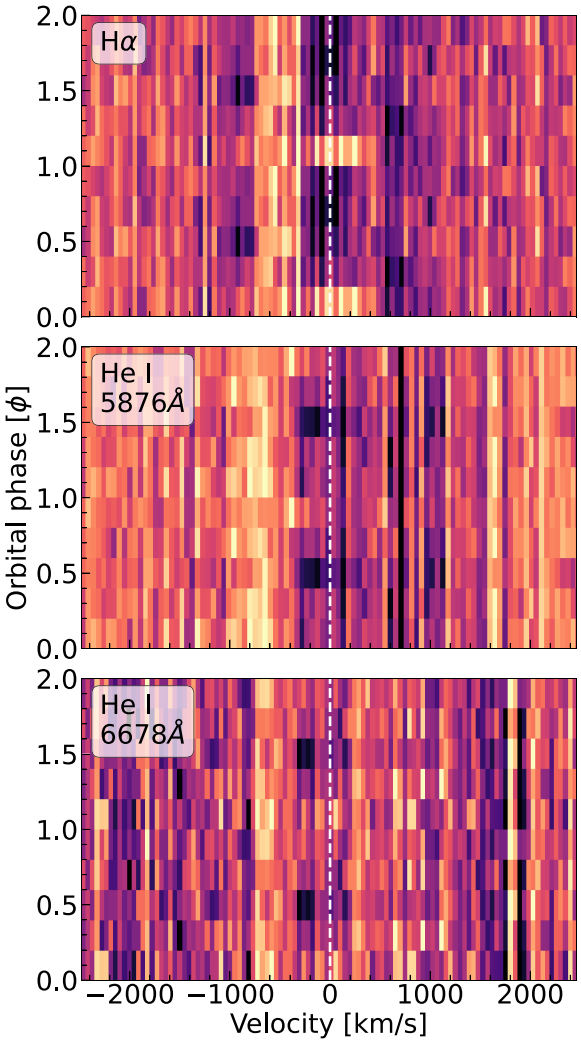

Figure 16. The phase-folded, trailed spectra of normalized lines in the GTC/R2500R spectra. We repeat the phase-folded spectra from phase 1 to 2. In the top panel we show the Hα line, in the middle panel the He I 5876 Å line, and in lower panel the He I 6678 Å line. The white vertical dashed lines indicate the rest velocity of each line. We plot the colourmap for each panel between the 1st and 99th quantile for clarity. We find that the strongest emission is apparent for all three lines around −600 km s^{-1}.

with the GTC observations, the modulation in the X-ray flux is also deepest around this orbital phase. Therefore, the broad absorption feature could potentially be related to the vertical structure suggested to partially obscure the X-ray emission. Furthermore, as we note substantial changes in the line profiles between the GTC and VLT spectra on a 5−6 d time-scale, this could potentially be related to the precession of the disc, which is suggested to cause considerable changes in the modulations in the light curves on day time scales as well (e.g. P. Hakala et al. 2005; P. A. Mason et al. 2008; P. Hakala et al. 2009).

The emission feature for the He I 6678 Å line is not clearly detected in the combined GTC spectrum. In the individual spectra, we do note a faint blue emission peak in some of the spectra. In the phase-folded, trailed spectrum, we can trace this emission feature as well. We also note hints of absorption around $\phi \approx 0.5$ in the trailed spectrum. For both the He I 5876 Å and He I 6678 Å, we only note a blue emission peak, both at a velocity of around −600 km s^{-1}. Notably,

the (stronger) blue emission peak is apparent for all three lines, and roughly constant in velocity over the orbital phase, as shown in Fig. 16. We will discuss this in the next section.

5 THE CASE FOR A DISC WIND AND POTENTIAL ASYMMETRY

In the presented data, we detect a blue-shifted absorption feature for the H β line in the GTC/R1000B spectrum. We also note hints of P-Cygni profiles in the Hβ line for the VLT data, as well as several features that could be naturally interpreted as being associated with a persistent disc wind. In this Section, we discuss and summarise these signatures, discuss these in context of a disc wind scenario, and explore its implications.

5.1 UV signatures tracing optically thin expanding material?

The goal of our work is to explore the nature of the UV outflow detected in S. Fijma et al. (2023). There the outflow was identified in the archival *HST* data through transient P-Cygni profiles in the Si IV 1400 Å line, and tentatively in the N V 1240 Å line. In our new *HST* exposures, we do not detect significant P-Cygni features in these lines, nor in other species. However, as discussed in Section 4.3, we note that Si IV 1400 Å appear substantially broader in the all exposures (archival and new) where no P-Cygni profiles are detected, and that this emission feature is never eclipsed in the orbit. This would be consistent with the Si IV 1394 Å and 1403 Å lines being formed above the disc in optically thin expanding material, as suggested for other LMXBs (see e.g. A. J. Bayless et al. 2010; T. Muñoz-Darias et al. 2016). This would suggest a persistent disc wind in UW CrB. Our results suggest we consistently detect the optically thin material above this disc, and only detect P-Cygni outflow signatures sporadically. This could be either due to a line-of-sight-effect (such as in P. Charles et al. 2019), clumping or density conditions of the wind (e.g. D. Mata Sánchez et al. 2018; T. Muñoz-Darias et al. 2019; A. Ambrifi et al. 2025), or changes in the ionization of the material (e.g. F. Jiménez-Ibarra et al. 2019; T. Muñoz-Darias et al. 2019).

We tested the latter option by measuring and comparing the relative line strengths of O IV 1343 Å and O V 1371 Å to probe changes in the ionization of the gas, as these are the only lines available to us in order to consistently compare with the archival observations described in S. Fijma et al. (2023). When comparing the archival exposures to our new exposures, we find that most of the new exposures have comparable values for ratio of the relative line strengths for O IV/O V as in the archival exposure where we detect the P-Cygni features, and some of the new exposures have comparable relative line strength the exposure preceding the P-Cygni detection. Therefore, we do not believe that ionization changes are responsible for not detecting UV P-Cygni signatures, and consider either line-of-sight effects or changes in density to be more likely.

5.2 P-Cygni features and asymmetries in optical lines

The persistent disc wind scenario is supported by our optical spectroscopy. First, the detection of a significant, blue-shifted absorption feature in the Hβ line, indicates an outflow in UW CrB. The terminal velocity of $\approx$1800 km s^{-1} traced by the line is slightly higher than the UV outflow detected in S. Fijma et al. (2023). This absorption feature is significantly detected in the single GTC/R1000B spectrum that we recorded at ϕ=0.67−0.82. However, we also note tentative blue-shifted absorption in the VLT data, which was identified in the time-averaged data over more than two source orbits. Therefore, we cannot draw conclusions on the transient or persistent nature, nor the phase-dependence of the outflow.

Notably, we detect clear blue-shifted absorption only in H β for the GTC/R1000B spectrum, and not in H α. M. R. Kennedy et al. (2024) also detect a P-Cygni profile only for H β and He I 5876 Å, and not in Hα, albeit at lower velocities ($\approx$500 km s^{-1}). As we note deep, broad absorption profiles for H α and He I 5876 Å, and as both lines have stronger emission profiles, this might complicate identifying clear blue-shifted absorption in these lines for this single GTC/R1000B spectrum.

We also find hints of transient P-Cygni features for the in He II 4686 Å line in UW CrB at around $\phi\approx$0.24−0.37. Similar features were recently detected as transient signatures for the first time in an LMXB (P. Charles et al. 2019; F. Jiménez-Ibarra et al. 2019) for the similarly short-period X-ray binary *Swift* J1357.2–0933 ($P_{\rm orb}$=2.8 h; e.g. J. M. Corral-Santana et al. 2013), showing that P-Cygni features can be produced by a dense, hot outflowing wind observed at a high (near edge-on) inclination.

Secondly, based on the trailed VLT and GTC data, we suggest that the H α and He II 4686 Å emission lines are partially formed above the disc, similar to Si IV 1400 Å. This could also suggest that part of the emission is formed in the wind, as suggested for the ADC X1822−371 (e.g. A. Somero et al. 2012), for the LMXB MAXI J1820−070 (K. I. I. Koljonen et al. 2023), and for CVs (J. H. Matthews et al. 2015). Alternatively, these features could also be produced by the rotationally dominated base of the wind, or the transition region near the base of the wind (K. I. I. Koljonen et al. 2023).

Thirdly, from the combined VLT exposures, we note asymmetric emission lines with both stronger blue (He II 4686 Å, Hδ) and red (Hα, Hβ, He I 10830 Å) emission peaks, as well as symmetric double peaked lines (He II 5411 Å, H γ). Asymmetric optical line profiles with stronger red peaks (and blue-shifted absorption) have been associated with disc wind outflows in LMXBs (e.g. T. Muñoz-Darias et al. 2016). If the H α and H β lines in the VLT data are absorbed by an outflow, which potentially also results in the tentative blue-shifted absorption for H β, this could be similar to the P-Cygni features detected for UW CrB in the FUV signatures in S. Fijma et al. (2023), as well as the blue-shifted absorption detected in the Hβ line in the GTC/R1000B spectrum.

Another way of interpreting the asymmetric line profiles, are disc hot spots or other asymmetric emission in the disc. In previous works, contributions of disc hot spots have been identified as a narrow emission line moving back and forth across the double disc component in orbital phase (e.g. R. J. Stover 1981; N. Castro Segura et al. 2021). For the combined line profiles, this could subsequently result in a stronger red or blue peak in the line profile. In our trailed spectra of UW CrB, we do not find evidence for such a component moving in orbital phase. The stronger peak appears consistently present over more than two source orbits, for both the strong blue peak in H α, He I 5876 Å and 6678 Å (see Fig. 16), and He II 4686 Å (see Fig. 14), as well as the slightly stronger red peak emission in the trailed H α spectra (see Fig. 13). Moreover, the different asymmetries recorded in different lines in the same (VLT) data set would argue against a disc hot spot origin, as the narrow component from a disc hot spot would be expected to cause the asymmetry with a similar velocity in the lines that are affected (as in e.g. R. J. Stover 1981). Therefore, we consider a disc hot spot origin for the asymmetric line profiles to be unlikely.

The stark differences in the relative peak strength and line profile for Hα between the GTC and VLT spectra could potentially be explained by a non-axisymmetric outflow, as briefly suggested in K. I. I. Koljonen et al. (2023) for the LMXB MAXI J1820+070. However, the line profiles could also be related to the complicated geometry of the system, as well as potential structures in the disc.

Overall, our UV and optical signatures are consistent with a persistent disc wind in UW CrB. S. Fijma et al. (2023) have shown that an accretion disc wind can be launched in the system, but they also consider alternative scenarios based on the orbital phase where the outflow was recorded. As our findings show that the outflow is not strictly orbital phase dependent, we are able to rule out these alternative scenarios, which we briefly discuss in Section 5.3.

5.3 Scenarios without a disc wind

In S. Fijma et al. (2023), two alternative outflow scenarios are presented based on the orbital phase where the UV outflow was detected ($\phi \approx 0.7-0.8$), namely ablation of the companion star or an outflow launched by the impact point from the accretion stream, or hot spot. As we do not consistently detect phase-dependent features, we consider an outflow from the impact point unlikely. M. R. Kennedy et al. (2024) suggest that the interaction between the wind and the impact region could give rise to P-Cygni detections at this phase and particular viewing angle, based on apparent P-Cygni profiles detected for Hβ and He I 5876 Å for UW CrB at phase $\phi \approx 0.6-1.14$.

For ablation, we might consider that the outflow does not need to be phase-dependent, and that potentially outflowing ablated material might be trailing the companion in the orbit (e.g. A. H. Knight et al. 2023; L. Rhodes et al. 2025). However, we argue that the ablation scenario is unlikely, due to the velocity of the outflow. Assuming the companion mass is around $M_2 \approx 0.2\,M_\odot$, and the radius is around $R_2 \approx 0.2\,R_\odot$ (e.g. S. L. Morris et al. 1990), the escape velocity is around $v_e \approx 618\,km\,s^{-1}$. When assuming the companion mass is around $M_2 \approx 0.1\,M_\odot$ as in P. Hakala et al. (2009), the escape velocity is around $v_e \approx 437\,km\,s^{-1}$. We can assume that the escape velocity v_e should correspond to the velocity of an ablation outflow, as this has been derived for black widow pulsars (e.g. S. Ginzburg & E. Quataert 2020, and references therein) with both wider and tighter orbital periods. The signatures in UW CrB that we believe trace the outflow in UV ($\approx 1500\,km\,s^{-1}$) and optical signatures (1300–1800 $km\,s^{-1}$) show much higher velocities than v_e for the companion star.

5.4 Orbital modulations due to a non-axisymmetric wind

As mentioned previously, the light curves of UW CrB show prominent modulations in all wavebands. Previous works have shown that a non-axisymmetric and/or elliptical accretion disc can be invoked to reproduce the variations in the optical light curves (e.g. P. A. Mason et al. 2008; P. Hakala et al. 2009). P. A. Mason et al. (2008) find that an elliptical disc model of $a_{disk} = 0.3a$ and $e = 0.5$, which precesses over a period of 5.5 d, creates reasonably comparable optical light curve. However, the orbital modulations in the X-ray light curves are more peculiar, and require an out-of-orbital-plane structure, as suggested by previous works (e.g. P. Hakala et al. 2005; P. A. Mason et al. 2008). This can potentially be attributed to a non-axisymmetric flared or warped accretion disc (e.g. P. Hakala et al. 2009; P. A. Mason et al. 2012) or non-axisymmetric disk wind as suggested by P. A. Mason et al. (2012).

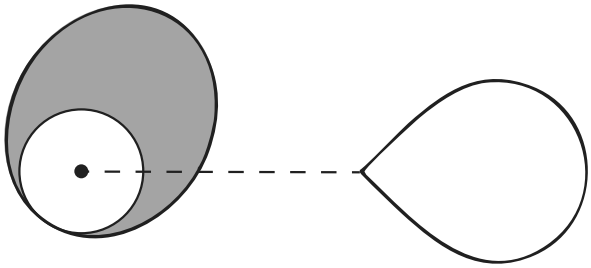

Figure 17. A schematic diagram showing the potential geometry of the elliptical accretion disk in UW CrB, as adapted from P. A. Mason et al. (2012). Here the disc is assumed to have an eccentricity of 0.5 and $a_{disc} = 0.3a$. In the shaded region, we show the regions of the disc exceeding 10 per cent of the Compton radius, which is where a thermal wind can be launched from the disc.

The latter scenario would be similar to wind observed in ADC source X1822−371 (e.g. C. Hellier & K. O. Mason 1989; A. J. Bayless et al. 2010; L. Burderi et al. 2010). In A. J. Bayless et al. (2010), they suggest the X-ray and optical orbital modulations they observe for X1822−371 can be explained by a optically thick base of the disc wind. From the optical and UV signatures of UW CrB, we think the out-of-orbital-plane structure would match well with an (optically thick) accretion disc wind or its base. Moreover, other scenarios such as a flared or warped accretion disc, are deemed unlikely, as radiation-induced warping is unlikely in a short-period LMXB like UW CrB (e.g. G. I. Ogilvie & G. Dubus 2001; P. Hakala et al. 2005) and might be insufficient to explain the light curves (e.g. A. J. Bayless et al. 2010). We note that the disc rim might still be impacted and raised by the stream from the companion star (e.g. L. Homer et al. 2001; P. Charles et al. 2019), although we would not expect this to result in a non-axisymmetric vertical structure.

The proposed peculiar disc geometry could naturally give rise to a non-axisymmetric disc wind as well. The elliptical disc model as proposed in P. A. Mason et al. (2012), is characterized by $a_{disk} = 0.3a$, $e = 0.5$, and the disc almost extending to the tidal truncation radius. The maximum and minimum distances of the disk edge from the neutron star are $0.3a(1 \pm e)$, or $0.45a$ and $0.15a$, respectively. To calculate the semi-major axis a for UW CrB, we use $P_{orb} = 110.98$ min, and we assume $M_1 = M_{NS} \approx 1.35 M_\odot$, and $M_2 = M_{CS} \approx 0.2 M_\odot$ (e.g. P. A. Mason et al. 2008). We find $a \approx 6.14 \times 10^{10}$ cm, so the maximum distance is $a_{max} = 0.45a \approx 2.7 \times 10^{10}$ cm, and the minimum distance is $a_{min} = 0.15a \approx 9 \times 10^9$ cm. The Compton radius is $R_{IC} \approx 9 \times 10^{10}$ cm (S. Fijma et al. 2023), and a thermal disc wind is expected to be launched and accelerated around $0.1R_{IC} \approx 9 \times 10^9$ cm (e.g. M. C. Begelman & C. F. McKee 1983; M. Díaz Trigo & L. Boirin 2016). This means that, when only considering thermal launching, the wind could likely only be launched in part of the disc. We show an adapted version of fig. 3 from P. A. Mason et al. (2012) in Fig. 17, where we show the regions exceeding $0.1R_{IC}$. This is assuming that the elliptical, precessing disc model presented in P. A. Mason et al. (2008) accurately describes the disc in UW CrB. Moreover, we note that this simple argument does not take radiation pressure due to electron scattering into account, which can enhance a thermal wind (e.g. R. Tomaru et al. 2018; N. Higginbottom et al. 2020).

5.5 Disc wind as the origin of the ADC

We argue that the out-of-plane structure causing the varying orbital modulations in the X-ray light curve could be the (base of) a cool,

optically thick, non-axisymmetric disc wind. In tracing the origin of the ADC, we also suggest that material from the accretion disc wind is reprocessing the X-ray emission in UW CrB. For ADC LMXBs, the medium scattering X-ray emission is under debate. M. C. Begelman & C. F. McKee (1983) originally suggested that winds could be scattering X-ray emission of ADC sources into the line of sight. This scenario was tested for the ADC source 2S 0921−630 by R. Tomaru et al. (2023). They conclude that emission lines in ADCs can be diffuse emission from scattering in a thermal-radiative wind. Moreover, a disc wind has also been detected previously in the ADC source X1822−371 (e.g. A. J. Bayless et al. 2010; L. Burderi et al. 2010), and previous works have suggested inefficient mass transfer due to a potential outflow for the ADC source 4U 2129+47 during its latest outburst in 1983 (e.g. M. A. Nowak, S. Heinz & M. C. Begelman 2002).

From our *XMM–Newton* EPIC-pn and RGS spectral analysis, we find clear emission lines, mostly between around 0.5–3 keV. This is likely due to the low absorption toward the source. The lack of emission line detections between 3−10 keV, i.e. where typically highly ionized iron lines are detected for ADC sources, is potentially limited due to the low SNR in our *XMM–Newton* data at these energies. Therefore, we cannot directly compare our spectrum to the work of R. Tomaru et al. (2023).

R. Tomaru et al. (2023) propose that one can trace the integrated velocity structure across all azimuths of the accretion disc wind through the width of the lines. Therefore, we measure the width of the N VII emission line in the RGS spectrum first order spectrum, as this is the only significant (4.6σ) emission line in the spectrum. We find $\sigma = 1400^{+400}_{-500}$ km s^{-1} (or a FWHM of 3300^{+900}_{-1200} km s^{-1}) of when fitting with a single Gaussian. This is consistent with the terminal velocity of the UV outflow in S. Fijma et al. (2023) of around 1500 km s^{-1}, and the velocity of the absorption edges of around 1300−1800 km s^{-1} for the Hβ and tentative He II 4686 Å optical blue-shifted absorption profiles. Therefore, our findings appear consistent with the origin of the ADC being a disc wind as well.

Finally, we note that the Fe Kα line profile appears to change in the flux-resolved spectra. If the line indeed consists of the Fe XXV 6.7 keV and Fe XXVI 6.97 keV lines, the line change can potentially be attributed to scattering (e.g. R. E. Shirey, A. M. Levine & H. V. Bradt 1999). Specifically, we might see a broad, red-skewed Fe Kα line because of the accretion disc wind (e.g. P. Laurent & L. Titarchuk 2007; L. Titarchuk, P. Laurent & N. Shaposhnikov 2009) and if the wind is indeed asymmetric, this might cause the observed changes in the Fe Kα line in orbital phase traced by the flux-resolved spectra. However, due to limitations in constraining the uncertainty on the width of the line in the EPIC-pn spectra, we cannot confirm this. Higher resolution phase-resolved X-ray spectroscopic observations could be used to confirm the presence of the two line components, and constrain their width.

5.6 Implications for binary evolution

Our preferred scenario of a persistent disc wind in UW CrB has important implications for binary evolution. If correct, it implies that mass transfer in persistently accreting NS-LMXBs can be highly non-conservative down to short orbital periods. As disc winds are proposed to remove high amounts of mass and angular momentum from the binary, this can impact the evolution of the orbit severely (e.g. G. Ponti et al. 2012; J. Neilsen 2013; J. M. Miller et al. 2015; N. Higginbottom et al. 2017; J. V. Hernández Santisteban et al. 2019). N. Castro Segura et al. (2024) have previously shown that disc winds can be persistent as opposed to flaring in transient NS-LMXBs with wider orbits. Moreover, the recent work of M. Gallegos-Garcia et al. (2024) has shown that disc winds are highly impactful for binary evolution prescriptions, as well as the rates and merger time for compact object binaries, and should be considered for population studies. Our work reinforces this, as it suggests that disc winds can be launched over a wider parameter space in orbital period and disc size than previously realized.

Our work incentivizes further exploration of disc winds in short-period X-ray binaries ($P_{\rm orb}$ <4 h), as these are currently under-represented in disc wind studies (e.g. M. Díaz Trigo & L. Boirin 2016; G. Panizo-Espinar et al. 2022; J. Neilsen & N. Degenaar 2023). As S. Fijma et al. (2023) show that heating from the NS compact object is needed to launch a wind in short-period X-ray binaries, and as most short-period LMXBs have a NS compact object, this leaves a prominent and important part of the parameter space to be explored.

We note that non-conservative mass transfer has also been inferred for accreting millisecond X-ray pulsars (AMXPs) (A. Marino et al. 2019), although strong jets or X-ray winds have not always been detected. Potentially, winds detectable in optical or UV signatures might contribute to the removal of mass and angular momentum in these systems.

The accretion disc wind in UW CrB is potentially asymmetric, as implied by the modulations in the X-ray light curves, as well as the predicted launching radius for a thermally driven wind. This could be interesting to explore in other short-period (NS)-LMXBs showing super-orbital variations as well. Our proposed scenario of a non-axisymmetric disc wind in UW CrB could be further strengthened by polarization observations, as an asymmetric disc wind is proposed to show a high degree of polarization (e.g. R. Tomaru, C. Done & H. Odaka 2024). Moreover, disc wind simulations including both thermal and radiative contributions would be valuable to determine the launching radius and physical properties of the disc wind in UW CrB.

6 SUMMARY AND CONCLUSIONS

In this work, we present a comprehensive multiwavelength campaign on the low-mass X-ray binary UW CrB, covering X-ray to radio wavelength. We summarize the conclusions as follows:

(i) In X-rays, we show the broad-band spectrum contains a variety of emission lines, which are well described using a model component producing a spectrum from a hot diffuse gas or optically thin plasma. This is consistent with its proposed characterization as an accretion disc corona source. The X-ray light curves show orbital modulations spanning more than half of the orbital period, which appear to be the result of an out-of-plane structure.

(ii) The multi-wavelength campaign was initiated based on transient P-Cygni outflow features detected in the far-UV Si IV and N V spectral lines by S. Fijma et al. (2023), suggesting the presence of a disc wind. In the new UV spectra, we do not detect similar P-Cygni profiles. However, we note that Si IV 1400 Å appears substantially broader in the all exposures (archival and new) where no P-Cygni profiles are detected, and that this emission feature is never eclipsed in the orbit. This would be consistent with the Si IV doublet being formed above the disc in optically thin expanding material.

(iii) The optical spectra are recorded with the VLT and GTC, separated by 5 d. For one of the GTC epochs, we identify blue-shifted absorption for the Hβ line, which might be the signature

of a disc wind outflow with a terminal velocity of $\approx$1800 km s^{-1}. Furthermore, we detect line asymmetries and identify tentative P-Cygni profiles in other epochs, which could be interpreted as being associated with a persistent disc wind.

(iv) We do not detect radio emission from UW CrB in the duration of our two week daily observing campaign with AMI-LA, obtaining a 3σ upper limit of 120 μJy at 15.5 GHz. The sampling and non-detections of these radio observations allows us to rule out that the intrinsic accretion rate is near-Eddington, i.e. it cannot be much higher than the proposed accretion rate o$L_X \approx 1$–10 per cent L_{EDD}.

(v) We discuss the results and the observed complex phenomenology in context of our preferred scenario of a persistent accretion disc wind. Our results suggest we consistently detect the optically thin material above this disc, and only detect P-Cygni outflow signatures sporadically, potentially due to line-of-sight-effects, clumping or density conditions of the wind. We also propose that the out-of-plane structure causing the varying orbital modulations in the X-ray light curve could be the (base of) a cool, optically thick, non-axisymmetric disc wind outflow, as the proposed peculiar disc geometry could give rise to a non-axisymmetric disc wind.

(vi) UW CrB is proposed to be an accretion disc corona source, meaning that the inner region and compact object are obscured, and subsequently all the X-ray emission is scattered into our line of sight, reducing the observed X-ray flux. Based on our results, we present a 'toy model' interpretation of the outflow scattering the X-ray emission into our line of sight.

(vii) Finally, we discuss the implications of our preferred scenario of a persistent disc wind in UW CrB. If correct, it implies that mass transfer in persistently accreting NS-LMXBs can be highly non-conservative down to short orbital periods. This is impactful for binary evolution prescriptions, and incentivizes further exploration of disc winds in short-period X-ray binaries.

ACKNOWLEDGEMENTS

We thank the anonymous referee for the valuable comments. We thank R. Fender, J. Matthews, J. Ontiveros, A. Ambrifi, P. Kosec, E. Caruso, A. Derkink, R. Wijnands for the helpful discussions. We thank C. Soto, L. Ballo, N. Patat, as well as the staff, telescope operators and scheduling teams of the *XMM–Newton*, *Swift*, *HST*, VLT, GTC, and AMI telescopes for scheduling, coordinating and performing the observations. We thank the staff of the Mullard Radio Astronomy Observatory, University of Cambridge, for their support in the maintenance, and operation of AMI.

SF and ND acknowledge the hospitality of the Instituto de Astrofísica de Canarias and the Texas Tech University, where part of this research was carried out. This paper is supported by European Union's 2020 research and innovation programme under grant agreement no. 871158, project AHEAD2020. SF gratefully acknowledges support from the Leids Kerkhoven–Bosscha Fonds (LKBF). NCS acknowledges support from the Science and Technology Facilities Council (STFC) grant ST/X001121/1. DMS acknowledges support by the Spanish Ministry of Science via the Plan de Generacion de conocimiento ID2020-120323GB-I00, as well as through a Ramon y Cajal Fellowship YC2023-044941. MAP acknowledges support through the Ramón y Cajal grant RYC2022-035388-I, funded by MCIU/AEI/10.13039/501100011033 and FSE+. JvdE was supported by funding from the European Union's Horizon Europe research and innovation programme under the Marie Skłodowska-Curie grant agreement no. 101148693 (MeerSHOCKS).

Based on observations obtained with *XMM–Newton*, an ESA science mission with instruments and contributions directly funded by ESA Member States and NASA. This work made use of data supplied by the UK Swift Science Data Centre at the University of Leicester. This research is based on observations made with the NASA/ESA *Hubble Space Telescope* obtained from the Space Telescope Science Institute, which is operated by the Association of Universities for Research in Astronomy, Inc., under NASA contract NAS 5–26555. These observations are associated with programe(s) 17272. Based on observations collected at the European Southern Observatory under ESO programme(s) 0111.D-2426(A). This work is based on observations made with the Gran Telescopio Canarias (GTC), installed at the Spanish Observatorio del Roque de los Muchachos of the Instituto de Astrofísica de Canarias on the island of La Palma, under programme GTC55-23A. The data were obtained with the OSIRIS instrument, built by a consortium led by the Instituto de Astrofísica de Canarias in collaboration with the Instituto de Astronomía of the Universidad Autónoma de México. OSIRIS was funded by GRANTECAN and the Spanish Government's National Plan for Astronomy and Astrophysics.

This research has made use of the SIMBAD data base, operated at CDS, Strasbourg, France. This work made use of NUMPY (C. R. Harris et al. 2020), and ASTROPY:[6] a community-developed core PYTHON package and an ecosystem of tools and resources for astronomy (Astropy Collaboration 2022).

DATA AVAILABILITY

The data underlying this article will be available in Zenodo at DOI: 10.5281/zenodo.15592504 upon publication. Most of the astrophysical data sets used in this work can be accessed from sources in the public domain, such as the XMM-Newton Science Archive (XSA; https://nxsa.esac.esa.int/nxsa-web/#search), the UK Swift Science Data Centre (https://www.swift.ac.uk/archive/index.php), the Mikulski Archive for Space Telescopes for Hubble (MAST; https://www.swift.ac.uk/archive/index.php), the ESO Science Archive Facility (SAF; https://archive.eso.org/cms.html), and the GTC archive (http://gtc.sdc.cab.inta-csic.es).

REFERENCES

Ambrifi A. et al., 2025, A&A, 694, A109
Arnaud K. A., 1996, in Jacoby G. H., Barnes J., eds, ASP Conf. Ser. Vol. 101, Astronomical Data Analysis Software and Systems V. Astron. Soc. Pac., San Francisco, p. 17
Astropy Collaboration, 2022, ApJ, 935, 167
Bandyopadhyay R. M., Shahbaz T., Charles P. A., Naylor T., 1999, MNRAS, 306, 417
Bayless A. J., Robinson E. L., Hynes R. I., Ashcraft T. A., Cornell M. E., 2010, ApJ, 709, 251
Begelman M. C., McKee C. F., 1983, ApJ, 271, 89
Blandford R. D., Payne D. G., 1982, MNRAS, 199, 883
Burderi L., Di Salvo T., Riggio A., Papitto A., Iaria R., D'Aì A., Menna M. T., 2010, A&A, 515, A44
Burrows D. N. et al., 2005, Space Sci. Rev., 120, 165
Carnall A. C., 2017, preprint (arXiv:1705.05165)
Castro Segura N. et al., 2021, MNRAS, 501, 1951
Castro Segura N. et al., 2022, Nature, 603, 52
Castro Segura N. et al., 2024, MNRAS, 527, 2508
Chakravorty S. et al., 2016, A&A, 589, A119
Charles P., Matthews J. H., Buckley D. A. H., Gandhi P., Kotze E., Paice J., 2019, MNRAS, 489, L47
Cohen J. G., Rosenthal A. J., 1983, ApJ, 268, 689

[6] http://www.astropy.org

Corral-Santana J. M., Casares J., Muñoz-Darias T., Rodríguez-Gil P., Shahbaz T., Torres M. A. P., Zurita C., Tyndall A. A., 2013, Science, 339, 1048
Cúneo V. A. et al., 2020, MNRAS, 498, 25
Degenaar N., Miller J. M., Harrison F. A., Kennea J. A., Kouveliotou C., Younes G., 2014, ApJ, 796, L9
Díaz Trigo M., Boirin L., 2016, Astron. Nachr., 337, 368
Done C., Gierliński M., Kubota A., 2007, A&A Rev., 15, 1
Dubus G., Kim R. S. J., Menou K., Szkody P., Bowen D. V., 2001, ApJ, 553, 307
Emmering R. T., Blandford R. D., Shlosman I., 1992, ApJ, 385, 460
Evans P. A. et al., 2007, A&A, 469, 379
Fender R. P., Maccarone T. J., van Kesteren Z., 2005, MNRAS, 360, 1085
Ferreira J., 1997, A&A, 319, 340
Fijma S., Castro Segura N., Degenaar N., Knigge C., Higginbottom N., Hernández Santisteban J. V., Maccarone T. J., 2023, MNRAS, 526, L149
Froning C. S. et al., 2011, ApJ, 743, 26
Fukumura K., Kazanas D., Shrader C., Behar E., Tombesi F., Contopoulos I., 2017, Nat. Astron., 1, 0062
Gallegos-Garcia M., Jacquemin-Ide J., Kalogera V., 2024, ApJ, 973, 168
Galloway D. K., Keek L., 2021, in Belloni T. M., Méndez M., Zhang C., eds, Astrophysics and Space Science Library Vol. 461, Timing Neutron Stars: Pulsations, Oscillations and Explosions. Springer, Berlin Heidelberg, p. 209
Georganti M. et al., 2025, preprint (arXiv:2501.17935)
Gill C. D., O'Brien T. J., 1999, MNRAS, 307, 677
Ginzburg S., Quataert E., 2020, MNRAS, 495, 3656
Gioia I. M., Henry J. P., Maccacaro T., Morris S. L., Stocke J. T., Wolter A., 1990, ApJ, 356, L35
Green J. C. et al., 2012, ApJ, 744, 60
HI4PI Collaboration, 2016, A&A, 594, A116
Hakala P., Ramsay G., Muhli P., Charles P., Hannikainen D., Mukai K., Vilhu O., 2005, MNRAS, 356, 1133
Hakala P., Hjalmarsdotter L., Hannikainen D. C., Muhli P., 2009, MNRAS, 394, 892
Hakala P. J., Chaytor D. H., Vilhu O., Piirola V., Morris S. L., Muhli P., 1998, A&A, 333, 540
Harris C. R. et al., 2020, Nature, 585, 357
Haswell C. A., Hynes R. I., King A. R., Schenker K., 2002, MNRAS, 332, 928
Hellier C., Mason K. O., 1989, MNRAS, 239, 715
Hernández Santisteban J. V. et al., 2019, MNRAS, 488, 4596
Hickish J. et al., 2018, MNRAS, 475, 5677
Higginbottom N., Proga D., Knigge C., Long K. S., 2017, ApJ, 836, 42
Higginbottom N., Knigge C., Long K. S., Matthews J. H., Parkinson E. J., 2019, MNRAS, 484, 4635
Higginbottom N., Knigge C., Sim S. A., Long K. S., Matthews J. H., Hewitt H. A., Parkinson E. J., Mangham S. W., 2020, MNRAS, 492, 5271
Homer L., Charles P. A., Hakala P., Muhli P., Shih I. C., Smale A. P., Ramsay G., 2001, MNRAS, 322, 827
Horne K., Marsh T. R., 1986, MNRAS, 218, 761
Hynes R. I., Robinson E. L., Jeffery E., 2004, ApJ, 608, L101
Icke V., 1980, AJ, 85, 329
Jiménez-Ibarra F., Muñoz-Darias T., Casares J., Armas Padilla M., Corral-Santana J. M., 2019, MNRAS, 489, 3420
Jonker P. G., van der Klis M., Kouveliotou C., Méndez M., Lewin W. H. G., Belloni T., 2003, MNRAS, 346, 684
Justham S., Schawinski K., 2012, MNRAS, 423, 1641
Kennedy M. R. et al., 2024, Open J. Astrophys., 8, 71
Knight A. H., Ingram A., Middleton M., Drake J., 2022, MNRAS, 510, 4736
Knight A. H., Ingram A., van den Eijnden J., Buisson D. J. K., Rhodes L., Middleton M., 2023, MNRAS, 520, 3416
Koljonen K. I. I., Long K. S., Matthews J. H., Knigge C., 2023, MNRAS, 521, 4190
Kuulkers E., van der Klis M., van Paradijs J., 1995, ApJ, 450, 748
Kuulkers E., Homan J., van der Klis M., Lewin W. H. G., Méndez M., 2002, A&A, 382, 947
Laurent P., Titarchuk L., 2007, ApJ, 656, 1056
Linares M. et al., 2010, ApJ, 719, L84
Marino A. et al., 2019, A&A, 627, A125
Mason P. A., Robinson E. L., Gray C. L., Hynes R. I., 2008, ApJ, 685, 428
Mason P. A., Robinson E. L., Bayless A. J., Hakala P. J., 2012, AJ, 144, 108
Mata Sánchez D. et al., 2018, MNRAS, 481, 2646
Mata Sánchez D. et al., 2022, ApJ, 926, L10
Matthews J. H., Knigge C., Long K. S., Sim S. A., Higginbottom N., 2015, MNRAS, 450, 3331
McMullin J. P., Waters B., Schiebel D., Young W., Golap K., 2007, in Shaw R. A., Hill F., Bell D. J., eds, ASP Conf. Ser. Vol. 376, Astronomical Data Analysis Software and Systems XVI. Astron. Soc. Pac., San Francisco, p. 127
Miller J. M., Raymond J., Fabian A., Steeghs D., Homan J., Reynolds C., van der Klis M., Wijnands R., 2006, Nature, 441, 953
Miller J. M., Fabian A. C., Kaastra J., Kallman T., King A. L., Proga D., Raymond J., Reynolds C. S., 2015, ApJ, 814, 87
Morris S. L., Liebert J., Stocke J. T., Gioia I. M., Schild R. E., Wolter A., 1990, ApJ, 365, 686
Muñoz-Darias T. et al., 2016, Nature, 534, 75
Muñoz-Darias T. et al., 2019, ApJ, 879, L4
Muhli P., Hakala P. J., Hjalmarsdotter L., Hannikainen D. C., Schultz J., 2004, in Tovmassian G., Sion E., eds, Revista Mexicana de Astronomia y Astrofisica Conference Series Vol. 20, Revista Mexicana de Astronomia y Astrofisica Conference Series. UNAM, Mexico, p. 211
Mukai K., Smale A. P., Stahle C. K., Schlegel E. M., Wijnands R., 2001, ApJ, 561, 938
Neilsen J., 2013, Adv. Space Res., 52, 732
Neilsen J., Degenaar N., 2023, preprint (arXiv:2304.05412)
Neilsen J., Lee J. C., 2009, Nature, 458, 481
Nowak M. A., Heinz S., Begelman M. C., 2002, ApJ, 573, 778
Ogilvie G. I., Dubus G., 2001, MNRAS, 320, 485
Oosterbroek T. et al., 1997, A&A, 321, 776
Özel F., Freire P., 2016, ARA&A, 54, 401
Panizo-Espinar G. et al., 2022, A&A, 664, A100
van Paradijs J., McClintock J. E., 1994, A&A, 290, 133
Penninx W., Lewin W. H. G., Zijlstra A. A., Mitsuda K., van Paradijs J., 1988, Nature, 336, 146
Perrott Y. C. et al., 2013, MNRAS, 429, 3330
Ponti G., Fender R. P., Begelman M. C., Dunn R. J. H., Neilsen J., Coriat M., 2012, MNRAS, 422, L11
Proga D., Kallman T. R., 2002, ApJ, 565, 455
Psaradaki I., Costantini E., Mehdipour M., Díaz Trigo M., 2018, A&A, 620, A129
Rahoui F., Coriat M., Lee J. C., 2014, MNRAS, 442, 1610
Ratti E. M., Steeghs D. T. H., Jonker P. G., Torres M. A. P., Bassa C. G., Verbunt F., 2012, MNRAS, 420, 75
Rhodes L., Russell D. M., Saikia P., Alabarta K., van den Eijnden J., Knight A. H., Baglio M. C., Lewis F., 2025, MNRAS, 536, 3421
Roming P. W. A. et al., 2005, Space Sci. Rev., 120, 95
Sánchez-Sierras J., Muñoz-Darias T., 2020, A&A, 640, L3
Shields G. A., McKee C. F., Lin D. N. C., Begelman M. C., 1986, ApJ, 306, 90
Shirey R. E., Levine A. M., Bradt H. V., 1999, ApJ, 524, 1048
Shlosman I., Vitello P. A., Shaviv G., 1985, ApJ, 294, 96
Siegel J. C. et al., 2023, ApJ, 954, 212
Smale A. P., 1998, ApJ, 498, L141
Somero A., Hakala P., Muhli P., Charles P., Vilhu O., 2012, A&A, 539, A111
Stover R. J., 1981, ApJ, 248, 684
Sztajno M., van Paradijs J., Lewin W. H. G., Langmeier A., Trumper J., Pietsch W., 1986, MNRAS, 222, 499
Tetarenko B. E., Lasota J. P., Heinke C. O., Dubus G., Sivakoff G. R., 2018, Nature, 554, 69
Titarchuk L., Laurent P., Shaposhnikov N., 2009, ApJ, 700, 1831
Tomaru R., Done C., Odaka H., Watanabe S., Takahashi T., 2018, MNRAS, 476, 1776
Tomaru R., Done C., Odaka H., Tanimoto A., 2023, MNRAS, 523, 3441
Tomaru R., Done C., Odaka H., 2024, MNRAS, 527, 7047
Ueda Y., Inoue H., Tanaka Y., Ebisawa K., Nagase F., Kotani T., Gehrels N., 1998, ApJ, 492, 782

Ueda Y., Murakami H., Yamaoka K., Dotani T., Ebisawa K., 2004, ApJ, 609, 325
Verner D. A., Ferland G. J., Korista K. T., Yakovlev D. G., 1996, ApJ, 465, 487
Wijnands R., Degenaar N., Armas Padilla M., Altamirano D., Cavecchi Y., Linares M., Bahramian A., Heinke C. O., 2015, MNRAS, 454, 1371
Wilms J., Allen A., McCray R., 2000, ApJ, 542, 914
Woods D. T., Klein R. I., Castor J. I., McKee C. F., Bell J. B., 1996, ApJ, 461, 767
Zwart J. T. L. et al., 2008, MNRAS, 391, 1545
van den Eijnden J. et al., 2021, MNRAS, 507, 3899

This paper has been typeset from a TEX/LATEX file prepared by the author.